Palladium-103 for Targeted Auger Electron Therapy: From Cyclotron Production and Innovative Separation to In Vivo Generator Evaluation and Preclinical Imaging

Thesis for the Degree of Doctor of Philosophy (PhD)

Aicha Nour Laouameria
Supervisor: Dr. Zoltán Szűcs

UNIVERSITY OF DEBRECEN
Doctoral Council for Natural Sciences and Engineering
Doctoral School of Chemistry
Debrecen, 2026

Hereby I declare that I prepared this thesis within the Doctoral Council for Natural Sciences and Engineering, Doctoral School of Chemistry, University of Debrecen in order to obtain a PhD Degree in Natural Sciences/ Engineering at Debrecen University.

The results published in the thesis are not reported in any other PhD theses.

Debrecen, 2026. January.

…….

Signature of the candidate

Hereby I confirm that **Aicha Nour Laouameria** candidate conducted her studies with my supervision within the K/4 Doctoral Program of the Doctoral School of Chemistry between 2022 and 2026. The independent studies and research work of the candidate significantly contributed to the results published in the thesis.
I also declare that the results published in the thesis are not reported in any other theses.
I support the acceptance of the thesis.

Debrecen, 2026. January.

……..

Signature of the supervisor

Palladium-103 for Targeted Auger Electron Therapy: From Cyclotron Production and Innovative Separation to In Vivo Generator Evaluation and Preclinical Imaging

Dissertation submitted in partial fulfilment of the requirements for the doctoral (PhD) degree
in Chemistry

Written by Aicha Nour Laouameria certified Chemist

Prepared in the framework of the doctoral school of chemistry of the University of Debrecen
(Macromolecular and Surface Chemistry (K4) program)

Dissertation supervisor: Dr. Zoltán Szűcs

The official opponents of the dissertation:

Dr. István Jószai
Dr. Homonnay Zoltán

The evaluation board:

chairperson:	Prof. Dr. Noémi Nagy
members:	Dr. .....
	Dr. .....
	Dr. .....
	Dr. .....

The date and venue of the dissertation defence: .. …….. 2026, HUN-REN Institute for Nuclear Research (ATOMKI), Debrecen, Hungary.

Acknowledgement

First and foremost, all praise and gratitude are due to Allah, the Almighty Creator, who granted me the opportunity to carry out this study and endowed me with the ability, strength, and knowledge to complete it successfully. I am sincerely grateful for His countless blessings and guidance throughout this journey, al-hamdu li-Allah.

I dedicate this work to my dear parents, Blidia Wahiba and Laouameria Mohamed, in recognition of their unconditional love, endless sacrifices, unwavering support, and heartfelt prayers throughout my studies. Thank you for always supporting my dreams.

My sincere acknowledgements go to my supervisor, Dr. Zoltán Szűcs, for his guidance, encouragement, and continuous support throughout all stages of this research. I am also very thankful to Dr. Mátyás Hunyadi for his support, collaboration, and valuable contributions. I further extend my gratitude to Dr. Domokos Máthé for his valuable collaboration, as well as to Dr. Attila Csík, and Dr. Mihály Braun for their collaboration and helpful scientific discussions. I also thank Dr. Brezovcsik Károly and Dr. Ferenc Ditrói for their assistance, and Prof. Dr. Béla Kovács for his collaboration.

I sincerely thank my dear sister Racha for her constant encouragement, moral support, and motivation, and my dear brothers Abd El Djalil for his moral encouragement and Kamar Eddine for his support. I would also like to thank my dear aunt Farida for her endless love and motivation, my beloved cousins Aram, Taeouil, and Adam, and my uncle Smail for his encouragement, as well as my aunts Lamia and Chahira. I remember with deep affection my late aunt Blidia Samia, whose kindness overwhelmed me and whose presence remains in my heart, and my late uncle Ournid Abd El Kader, with whom I

shared my dreams and goals. May Allah have mercy on them both. I am also grateful to my closest friends Hana, Amel, and Aya, with whom I shared the challenges and achievements of the past four years of my PhD research. Your friendship and support made this journey more meaningful.

I gratefully acknowledge the HUN-REN Institute for Nuclear Research (ATOMKI) and all its kind and professional staff members for their assistance during my studies and research, and for creating a supportive and friendly working environment. I also express my appreciation to the members of the Doctoral School of Chemistry, University of Debrecen, for their assistance. This research was supported by the Stipendium Hungaricum Scholarship Programme of the Hungarian Government. Furthermore, this work was supported by the project TKP2021-NKTA-42, financed by the National Research, Development and Innovation Fund of the Ministry for Innovation and Technology, Hungary.

Table of Contents

Abbreviations

The following abbreviations are used in this thesis:

ALD	Atomic layer deposition
AMBA	Aminomethylbenzoic acid
BEM	Beam energy monitor
CGM	Continuous Glucose Monitoring
CT	Computed tomography
DOTA	1,4,7,10-tetraazacyclododecane-1,4,7,10-tetraacetic acid
DOTA-TATE	DOTA-[Tyr^3]-octreotate
DOTA-TOC	DOTA-[Tyr^3]-octreotide
DSB(s)	Double-Strand Break(s)
EC	Electron Capture
EDS	Energy-dispersive X-ray spectroscopy
EGFR	Epidermal Growth Factor Receptor
EOB	End of Bombardment
ESTAR	Electron Stopping Powers and Ranges
HPGe	High-Purity Germanium detector
IC	Internal Conversion
ICP-MS	Inductively coupled plasma mass spectrometry
IGF-2	Insulin-like Growth Factor-2
iTLC	Instant Thin-Layer Chromatography
LET	Linear Energy Transfer
MAA	Macro-aggregated albumin
MIP	Maximum intensity projection
NHS	N-Hydroxysuccinimide

NOTA	1,4,7-Triazacyclononane-1,4,7-triacetic acid
PRRT	Peptide Receptor Radionuclide Therapy
p.i.	post-injection
QMA	Quaternary methyl ammonium
RCP	Radiochemical Purity
RSE	Radionuclide Separation Equipment
SD	Standard Deviation
SEM	Scanning electron microscopy
SNMS	Secondary neutral mass spectrometry
SPE	Solid-Phase Extraction
SPECT	Single-photon emission computed tomography
SSB(s)	Single-Strand Break(s)
SSTR2	Somatostatin Receptor Subtype 2
TENDL	TALYS-based Evaluated Nuclear Data Library
TRNT	Targeted Radionuclide Therapy
YSZ	Yttria-Stabilized Zirconia

I. Introduction

Radiopharmaceutical therapy aims to deliver radiation selectively to tumor cells while sparing healthy tissue, thereby minimizing off-target toxicity and enhancing therapeutic efficacy. Targeted radionuclide therapy (TRNT) offers an advanced approach in cancer treatment by localising cytotoxic radiation to tumor tissues with high specificity [1]. Conventional radionuclide therapies often employ beta (β)-emitters and alpha (α)-emitters (e.g., Lutetium-177 (^{177}Lu) or Actinium-225 (^{225}Ac)) [2, 3], which release high-energy particles that deposit dose over millimeters, sufficient for treating bulky tumors, but frequently causing collateral damage in surrounding healthy tissue [4]. Such limitations motivate the search for radionuclides capable of delivering radiation with subcellular precision to better target minimal residual disease, disseminated tumor cells, or micrometastases.

Auger electron–emitting radionuclides have emerged as promising candidates for such precision therapy [5]. As a result of the decay processes of these radionuclides, a series of low-energy electrons are ejected in what is referred to as the Auger effect [6], with nanometer-scale penetration ranges, leading to extremely localized dose deposition, often within a few tens of nanometers [7, 8]. This short-range deposition can induce lethal DNA damage when the radionuclide is placed in close proximity to the cell nucleus, thereby minimizing exposure of neighboring healthy cells [9]. The Auger effect is based on the emission of an electron following various excitation processes, such as electron capture (EC), internal conversion (IC), or photoelectric X-ray absorption [10]. The energy released by β^--emitting radionuclides is typically sufficient only to induce single-strand DNA breaks (SSBs), whereas both α-particles and Auger electrons are capable of producing double-strand breaks

(DSBs) [11, 12]. Cells are generally able to recognize and repair single-strand breaks [13], but DSBs represent a critical form of damage that often leads to apoptosis or irreversible loss of viability [14]. Similar to nuclear DNA damage, high-dose irradiation of mitochondria is also lethal for the cell, and this effect can only be achieved by radiation with sufficiently high linear energy transfer (LET). Alpha particles exhibit the highest LET (50–230 keV/µm), while Auger electrons fall into an intermediate LET range (4–26 keV/µm), significantly higher than that of beta particles (≈ 0.2 keV/µm) (Figure 1) [15].

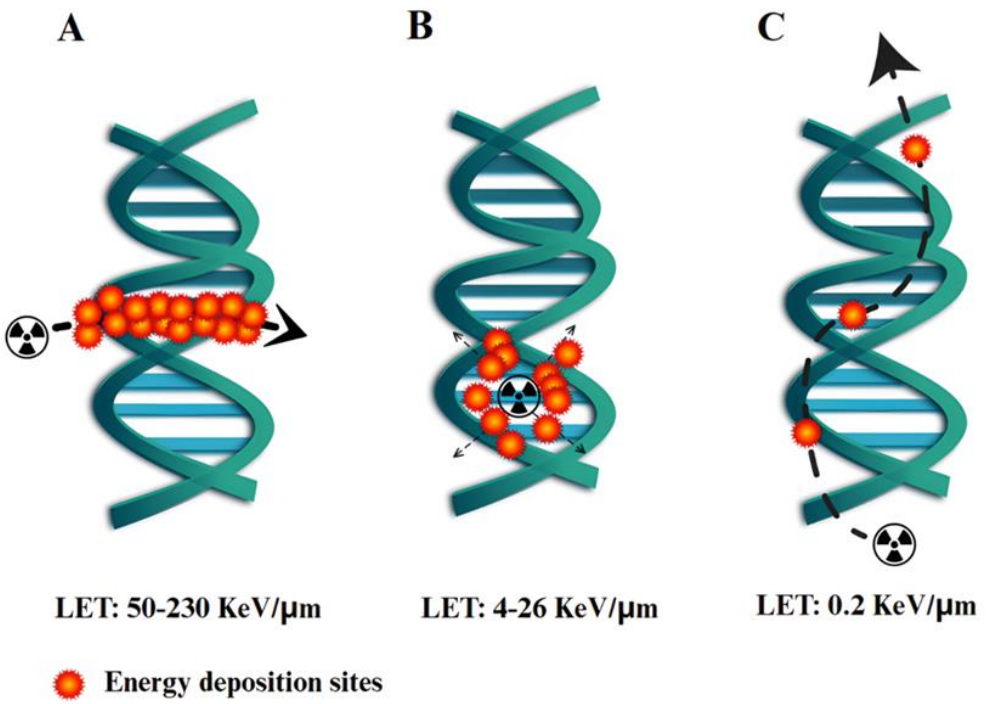

Figure 1. Comparison of Radiation Emissions: (**A**) Alpha particles; (**B**) Auger electrons; and (**C**) Beta particles. LET: Linear Energy Transfer.

Despite not reaching the LET values of α-emitters, an important advantage of Auger electron emitters over α-emitting radionuclides for tumor therapy is their extremely short penetration range, which makes them uniquely

capable of inducing double-strand DNA breaks (DSBs) while sparing adjacent healthy tissue. For instance, simulations using Geant4-DNA have demonstrated that Auger electron emitters can produce multiple DSBs, underscoring their potential in targeted cancer therapy [16]. These results substantiate that Auger electron therapy can effect potent subcellular damage supporting its therapeutic potential. In contrast, α-particles travel across several cell diameters, thereby exposing adjacent healthy tissue to collateral damage.

Within this class, palladium-103 (^{103}Pd) stands out due to its dual radiophysical properties: it emits γ photons suitable for imaging, while simultaneously providing Auger electrons for cytotoxicity, suggesting a theranostic potential [17]. ^{103}Pd decays by electron capture (EC) with a half-life of 16.99 days (Figure 2a), to rhodium-103 metastable state (^{103m}Rh) ($t_{1/2}$ = 56.1 minutes (min)), which undergoes isomeric transition to stable rhodium-103 (^{103}Rh) with the emission of additional Auger electrons and low-intensity gamma(γ)-rays [18, 19]. This process leaves a core–hole state that recombines via deexcitation cascades emitting characteristic X-rays (K-edge at 24.37 keV) and Auger electrons with a branching ratio of 77% and 23%, respectively [20]. From a technical point of view, the relatively low energy of X-ray photons allows for the non-problematic shielding, handling, storage, and elution of a ^{103}Pd-based generator [21].

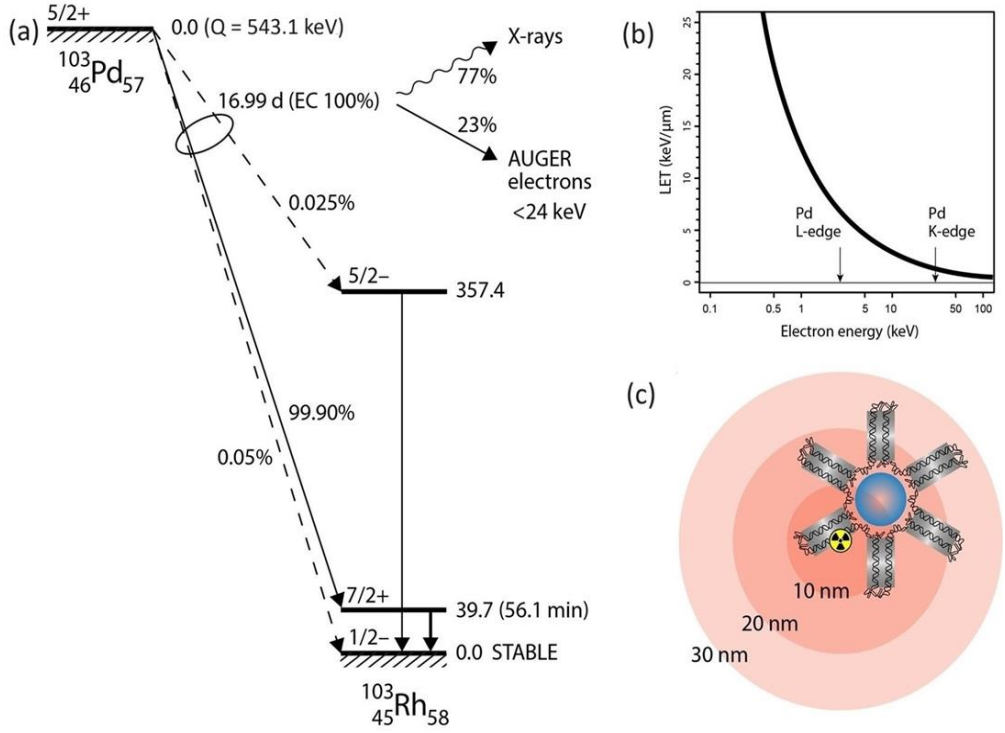

Figure 2. (**a**) Decay scheme of ^{103}Pd showing the subsequent decay of core–hole states via characteristic X-ray and Auger electrons; (**b**) Stopping power of electrons in an exemplary organic medium (guanine) for the energy range of typical Auger electrons calculated via the ESTAR code [22]; (**c**) Illustration of impact range of Auger electrons compared to the dimensions of chromatin strands.

In Auger transitions, a cascade process is generated via the deexcitation of the initial deep hole state. During this process, numerous low-energy electrons are emitted with a few hundred eV, which have a steeply increasing stopping power (LET) with decreasing energy (Figure 2b). These low-energy electrons have a stopping range of 30–50 nm, comparable with the average diameter of chromatin strands (~30 nm), as illustrated in Figure 2c. However, despite the theoretical advantages, translation of ^{103}Pd into targeted radionuclide therapy has been limited, partly owing to challenges in its production and radiochemical processing.

The production of ^{103}Pd from stable ^{103}Rh using a cyclotron has been reported, mainly through the ^{103}Rh(p,n)^{103}Pd reaction [23, 24]. Furthermore, an Auger electron emitter should be produced via a low-cost process while maximizing specific activity and purity to present therapeutic potential [25, 26]. However, the separation process of the ^{103}Pd from rhodium targets remains challenging and is usually carried out via wet chemistry, which is plagued by rhodium's high chemical inertness, leading to low yields, long processing times, substantial radioactive waste, and difficulties scaling up [27], all of which hamper routine production for preclinical or clinical use.

To overcome these limitations, diffusion-driven dry-distillation techniques have been proposed as an alternative separation strategy [28, 29]. This approach exploits intrinsic differences in partial vapor pressures between palladium (Pd) and rhodium (Rh) at elevated temperatures, enabling selective volatilization of ^{103}Pd from irradiated rhodium foils. Initial proof-of-concept studies demonstrated the feasibility of this method and laid the foundation for further technical optimization. Together with a novel substrate-based recovery method, this approach enabled efficient, scalable, and reproducible separation and purification of cyclotron-produced ^{103}Pd, with the possibility of reusing target materials, a feature that improves cost-effectiveness and sustainability.

Beyond radionuclide production and separation, a critical consideration for Auger electron–emitting radionuclides is the stability of daughter radionuclides following radioactive decay. In this context, the ^{103}Pd/^{103m}Rh parent–daughter pair is of particular interest as a potential in vivo generator system [30]. In the present study, the experimental release of free daughter ions was systematically investigated in the ^{103}Pd/^{103m}Rh parent–daughter system. This investigation is highly relevant because both radionuclides are pure Auger electron emitters and thus offer the potential for

a dual therapeutic effect when ^{103}Pd is employed in targeted applications, provided that the daughter radionuclide remains confined to the biological target defined by the vector molecule. Such radionuclide pairs, commonly referred to as in vivo generators, are regarded as particularly promising candidates for targeted radionuclide therapy due to their ability to deliver multiple localized decay events from a single targeting event [31].

In terms of clinically relevant chelators, DOTA is a widely applied chelator owing to its ability to form stable complexes with a broad range of radiometals. In peptide receptor radionuclide therapy (PRRT), somatostatin receptor–targeting bioconjugates such as DOTA-TOC (DOTA-[Tyr^3]-octreotide) are routinely radiolabeled for the treatment of neuroendocrine tumors [32]. The DOTA-TOC chelator–peptide therefore provides a robust and clinically established platform for evaluating daughter radionuclide release in an in vivo generator system, particularly as such investigations have not yet been systematically performed. This study quantitatively evaluates the release of the ^{103m}Rh daughter radionuclide from ^{103}Pd–chelator complexes and examines the relationship between the fraction of free daughter ions and the underlying Auger electron emission processes. In parallel, the associated biological implications of daughter radionuclide release are assessed by considering decay characteristics, half-life, potential cellular transport mechanisms, and the broader consequences of localized versus delocalized radiation exposure.

Moreover, while previous efforts have largely focused on brachytherapy applications or theoretical dosimetry, systematic in vivo evaluation of ^{103}Pd radiolabeled constructs remains scarce. Preclinical imaging and biodistribution studies are essential to validate the chemical stability, pharmacokinetics, and targeting behavior of ^{103}Pd conjugates.

Accordingly, this study extends beyond radiochemistry and evaluate [^{103}Pd]Pd–NOTA and [^{103}Pd]Pd–DOTA-TATE complexes in murine models, and explore a translational large-animal (canine) model with spontaneous liver cancer, to assess both imaging feasibility and preliminary therapeutic potential (Figure 3).

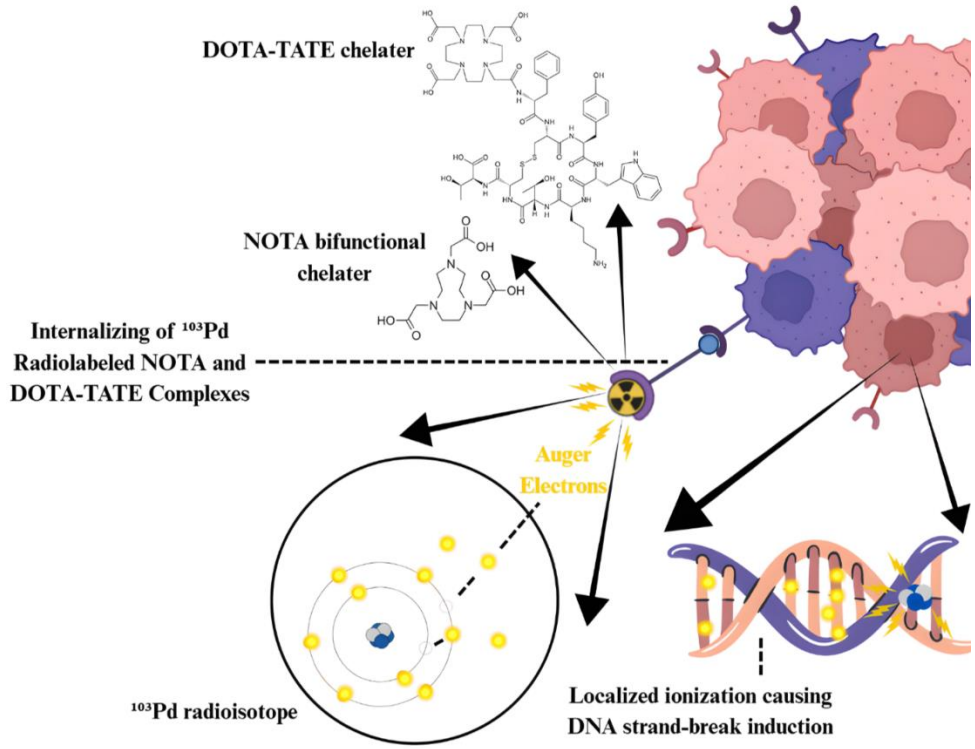

Figure 3. Mechanism of cellular delivery and Auger electron–induced cytotoxic effects of ^{103}Pd-radiolabeled NOTA and DOTA-TATE complexes.

The bifunctional chelator 1,4,7-triazacyclononane-1,4,7-triacetic acid (NOTA) was conjugated to primary amine–containing biomolecules using standard NHS ester chemistry [33], providing efficient and site-specific chelator attachment; notably, this work supposed to represent the first reported radiolabeling of NOTA with ^{103}Pd. In parallel, DOTA-TATE (DOTA-[Tyr^3]-octreotate) was employed as a clinically established somatostatin receptor

subtype-2 (SSTR2)–targeting vector with proven applicability in peptide receptor radionuclide therapy. Although [^{103}Pd]Pd–labeled DOTA-TATE has not previously been reported, the well-documented chelation properties of DOTA [34, 35] and the favorable radiochemical behavior of ^{103}Pd support its potential as a theranostic Auger electron–emitting agent.

Accordingly, the present work aims to establish and validate a complete, scalable workflow for the cyclotron production, dry-distillation separation, recovery, purification, radiolabeling, and preclinical evaluation of ^{103}Pd. In addition, this study provides a systematic experimental assessment of daughter radionuclide release in the ^{103}Pd/^{103m}Rh in vivo generator system and evaluates its implications for biological safety and therapeutic applicability. By integrating nuclear physics, materials science, radiochemistry, and in vivo imaging, this research seeks to position ^{103}Pd as a compelling candidate for targeted Auger electron–based theranostic applications.

II. Research objectives

The overarching objective of this PhD research is to establish and validate palladium-103 as a theranostic Auger electron–emitting radionuclide for targeted radionuclide therapy through the development of an integrated, scalable, and efficient production–to–preclinical evaluation workflow.

To achieve this overarching goal, the specific objectives of this research are:

1. **To optimize the cyclotron production of ^{103}Pd** via the ^{103}Rh(p,n)^{103}Pd nuclear reaction by identifying irradiation parameters that maximize production yield while maintaining high radionuclidic purity.
2. **To investigate palladium–rhodium interdiffusion mechanisms** through controlled multilayer experiments and depth-profiling analysis, and to determine diffusion coefficients relevant to the dry-distillation separation process.
3. **To design, construct, and optimize a diffusion-driven dry-distillation radionuclide separation equipment (RSE)** capable of selectively separating ^{103}Pd from irradiated rhodium targets by exploiting intrinsic differences in vapor pressure, thereby providing a robust alternative to conventional wet-chemistry separation methods.
4. **To enhance separation efficiency and recovery yield** through systematic optimization of RSE operational parameters, deposition substrates, and recovery methodologies, while ensuring the structural integrity and reusability of rhodium target foils.

5. **To quantify residual (cold) palladium in rhodium foils before and after RSE treatment** using ICP-MS, and to evaluate the impact of pre-irradiation palladium removal on the achievable specific activity of cyclotron-produced ^{103}Pd.

6. **To assess the radionuclidic purity and activity of separated ^{103}Pd** using high-resolution γ-spectroscopy and ionization chamber measurements throughout the separation and recovery workflow.

7. **To investigate the release dynamics of the daughter radionuclide ^{103m}Rh** from chelator-bound [^{103}Pd]Pd–DOTA-TOC complexes in the ^{103}Pd/^{103m}Rh in vivo generator system, and to quantify daughter release fractions in relation to Auger electron emission processes.

8. **To assess the therapeutic and safety implications of Auger electron emission and daughter radionuclide release**, integrating nuclear decay physics, radiochemistry, and biological considerations to evaluate the feasibility of ^{103}Pd for targeted Auger electron–based theranostic applications.

9. **To evaluate the radiochemical stability and chelation behavior of ^{103}Pd** using clinically relevant chelators (NOTA and DOTA-TATE), including quality control, and stability assessment.

10. **To perform preclinical in vivo evaluation of ^{103}Pd-radiolabeled constructs**, including biodistribution and SPECT/CT imaging in murine models and translational assessment in a spontaneous canine cancer model.

III. Literature review

III.1. Targeted Radionuclide Therapy

Targeted radionuclide therapy is an established and rapidly evolving modality in nuclear medicine that aims to selectively deliver cytotoxic radiation to malignant tissues while minimizing irradiation of surrounding healthy organs. Unlike external beam radiotherapy, TRNT exploits systemically administered radiopharmaceuticals that combine a radionuclide with a biological targeting vector, such as peptides, antibodies, antibody fragments, or small molecules, to achieve molecular-level specificity based on receptor expression, metabolic pathways, or tumor microenvironment characteristics [36].

The fundamental principle of TRNT is the spatial confinement of radiation dose to tumor cells through selective accumulation and retention of the radiopharmaceutical at the disease site. This approach enables treatment of disseminated disease, micrometastases, and minimal residual tumors that are inaccessible to surgical intervention or localized external irradiation [37]. The success of TRNT therefore depends on a delicate interplay between radiophysical properties of the radionuclide, radiochemical stability of the radiopharmaceutical, biological targeting efficiency, and in vivo pharmacokinetics.

Historically, TRNT has been dominated by β^--emitting radionuclides, including yttrium-90 (^{90}Y) and lutetium-177 (^{177}Lu), which have demonstrated clinical efficacy in several malignancies. PRRT using [^{177}Lu]Lu–labeled somatostatin analogues, such as [^{177}Lu]Lu–DOTA-TATE, represents a milestone in the treatment of neuroendocrine tumors and is now widely adopted in clinical practice [38-41]. β^--emitters offer favorable production

routes, established radiochemistry, and sufficient tissue penetration to treat bulky tumors. However, the millimeter-range path length of β^- particles leads to cross-fire irradiation of healthy tissues, which can result in dose-limiting toxicities to organs such as the kidneys, bone marrow, and liver [42]. While this cross-fire effect can be beneficial in heterogeneous tumors, it inherently limits the precision of dose deposition at the cellular and subcellular levels.

More recently, α-emitting radionuclides, including actinium-225 and radium-223 (^{223}Ra), have gained considerable attention due to their extremely high linear energy transfer (LET) and potent cytotoxicity [43, 44]. Alpha particles deposit large amounts of energy over a very short range, inducing complex DNA double-strand breaks that are difficult for cells to repair. Clinical successes with ^{223}Ra- and ^{225}Ac-based radiopharmaceuticals have demonstrated the powerful therapeutic potential of α-emitters. Despite these advantages, α-therapy is associated with significant challenges. These include limited radionuclide availability, complex decay chains, and the recoil-induced release of daughter radionuclides, which can cause unintended redistribution and off-target toxicity [45, 46]. Furthermore, the long particle range relative to cellular dimensions can still expose adjacent normal cells, particularly in tissues with high physiological uptake.

In light of these limitations, increasing attention has been directed toward radionuclides capable of delivering highly confined energy deposition at the cellular and subcellular levels. Among these, Auger electron–emitting radionuclides have emerged as a distinct class of therapeutic agents, offering the potential for nanometer-scale irradiation provided that sufficient intracellular and ideally intranuclear localization can be achieved. This has led to the development of Auger electron therapy as a complementary strategy within the broader framework of targeted radionuclide therapy.

III.2. Auger Electron Therapy

Auger electron therapy has emerged as a highly promising extension of targeted radionuclide therapy, particularly in response to the intrinsic limitations of β^-- and α-emitting radiopharmaceuticals in achieving subcellular dose confinement. Recent comprehensive reviews have emphasized that low-energy electron–emitting radionuclides, including Meitner–Auger emitters, offer unique therapeutic advantages due to their ability to deposit radiation energy over nanometer-scale dimensions, provided appropriate intracellular localization can be achieved [47, 48]. These properties make Auger emitters especially attractive for applications targeting micrometastatic disease, minimal residual tumors, and heterogeneous cellular populations where cross-fire irradiation is undesirable.

While early Auger electron therapy concepts focused predominantly on nuclear DNA damage, accumulating experimental evidence indicates that the biological effectiveness of Auger electron emitters is not exclusively dependent on direct DNA strand break induction. Auger electron cascades can induce significant extranuclear cytotoxic effects through interactions with critical cellular structures, including mitochondrial membranes and protein–cofactor complexes involved in oxidative phosphorylation. Disruption of these systems can impair cellular metabolism, increase oxidative stress, and activate regulated cell death pathways such as apoptosis and ferroptosis [49-51]. These mechanisms are particularly relevant in cancer cells, which often exhibit altered redox balance and mitochondrial dysfunction, rendering them more susceptible to localized oxidative damage.

In addition, Auger electron–induced lipid peroxidation has been identified as an important contributor to cytotoxicity. Low-energy electrons

can initiate radical-mediated membrane damage, leading to loss of membrane integrity and downstream signaling events associated with cell death. Such effects may complement direct radiotoxicity and further enhance therapeutic efficacy, especially in tumors with compromised antioxidant defenses. Moreover, emerging data suggest that Auger electron irradiation may elicit non-targeted biological responses, including bystander and immunomodulatory effects, which could enhance tumor control through activation of immune effector mechanisms [47].

Despite their favorable radiobiological characteristics, the clinical translation of Auger electron emitters remains strongly dependent on radionuclide availability, production feasibility, achievable specific activity, and radiochemical stability. Systematic evaluations of candidate radionuclides have highlighted that these practical considerations are as critical as decay characteristics when selecting suitable Auger emitters for therapeutic applications [52]. In this context, Auger electron therapy is increasingly viewed not as a replacement but as a complementary strategy to established β^-- and α-based therapies, particularly where extreme dose localization is required and off-target toxicity must be minimized [48].

Finally, advances in radiopharmaceutical design including optimized chelation strategies, peptide-based targeting vectors, and pharmacokinetic modulation, have further expanded the applicability of Auger emitters. Studies employing somatostatin receptor–targeting constructs and albumin-binding radioligands illustrate how established targeting platforms can be adapted to evaluate new radionuclide systems and improve tumor retention [53, 54]. Collectively, these developments underscore the growing relevance of Auger electron therapy within the broader framework of targeted radionuclide

therapy and provide a strong rationale for continued investigation of suitable Auger electron-emitting radionuclides.

III.3. Palladium-103 as an Auger Electron–Emitting Radionuclide

Palladium-103 is a well-characterized radionuclide that has attracted renewed interest as a candidate for Auger electron–based targeted radionuclide therapy due to its favorable decay properties, manageable photon emissions, and established production routes. The radiophysical characteristics of ^{103}Pd are particularly well suited for Auger electron therapy. The majority of its emitted electrons possess energies in the sub-keV to few-keV range, resulting in extremely short path lengths on the nanometer scale. Consequently, the deposited radiation dose is highly localized, minimizing cross-fire effects and reducing irradiation of adjacent healthy tissue. In addition to Auger electrons, ^{103}Pd emits γ-rays [55], which are sufficiently penetrating for external detection while remaining compatible with straightforward radiation shielding requirements [56].

Clinically, ^{103}Pd has a long history of use in permanent interstitial brachytherapy, particularly for prostate cancer, where its low photon energy contributes to favorable dose distributions and reduced exposure to surrounding organs at risk. This established clinical precedent demonstrates the radiological safety, manufacturability, and regulatory familiarity of ^{103}Pd, providing a strong foundation for its further development in targeted radiopharmaceutical applications beyond brachytherapy [57, 58].

From a theranostic perspective, ^{103}Pd offers a rare combination of properties that enable both therapy and imaging within a single radionuclide system. While its Auger electron emissions provide the cytotoxic component required for highly localized cell killing, the accompanying X-ray emissions

allow for non-invasive imaging, quality control, and longitudinal monitoring of biodistribution using SPECT-based techniques. This dual functionality supports individualized treatment planning and real-time assessment of radiopharmaceutical behavior in vivo, which are increasingly recognized as essential components of precision nuclear medicine [6, 59].

The decay of ^{103}Pd to ^{103m}Rh further introduces the concept of an in vivo generator system, in which the daughter radionuclide contributes additional Auger electron emissions following isomeric transition. Although the recoil energy associated with electron capture decay is low, experimental studies have demonstrated that chemical destabilization induced by Auger electron cascades may lead to partial release of the daughter nuclide from the coordination environment. This phenomenon has important implications for radiopharmaceutical design, chelation chemistry, and biological safety, and motivates systematic investigation of the ^{103}Pd/^{103m}Rh system in targeted applications [60].

Taken together, the favorable half-life, low-energy electron emissions, clinically validated photon characteristics, and theranostic potential position ^{103}Pd as a compelling candidate for Auger electron therapy. When combined with appropriate targeting vectors and robust chelation strategies, ^{103}Pd enables highly localized dose delivery while maintaining imaging capability and translational feasibility. These attributes justify continued interest in its production, separation, and radiopharmaceutical development, as explored in the subsequent sections of this work.

III.4. Production Routes of Palladium-103

Palladium-103 is a well-established medical radionuclide whose production routes have been extensively investigated due to its long-standing

clinical use in brachytherapy and its emerging potential as an Auger electron emitter for targeted radionuclide therapy. The selection of an appropriate production method is governed by several critical factors, including achievable yield, radionuclidic purity, specific activity, target material availability, irradiation infrastructure, and downstream radiochemical processing requirements [61, 62].

Historically, ^{103}Pd has been predominantly produced in nuclear reactors [63], usually via neutron-induced reactions on enriched palladium or rhodium targets. One established route involves the ^{102}Pd(n,γ)^{103}Pd reaction using highly enriched ^{102}Pd targets [64]. This method benefits from relatively high production yields and straightforward irradiation procedures. However, the resulting product typically exhibits low specific activity due to the presence of stable palladium carrier, which limits its suitability for applications requiring high molar activity, such as receptor-targeted radiopharmaceuticals [65].

Cyclotron production of ^{103}Pd has attracted increasing attention due to its potential to deliver higher specific activity products and to leverage widely available medical cyclotrons. The most extensively studied and practically relevant charged-particle reaction is the ^{103}Rh(p,n)^{103}Pd reaction [23, 66]. This route offers several advantages, including the use of monoisotopic natural rhodium targets, relatively high cross-sections at low-to-moderate proton energies, and favorable radionuclidic purity when irradiation parameters are carefully optimized.

Experimental excitation function measurements have demonstrated that the ^{103}Rh(p,n)^{103}Pd reaction exhibits a broad cross-section maximum in the proton energy range of approximately 10–15 MeV [67, 68]. Operating

within this energy window allows efficient production while minimizing the co-production of unwanted palladium or rhodium isotopes, which may compromise radionuclidic purity [69].

Additional charged-particle routes, including deuteron-induced reactions such as ^{103}Rh(d,2n)^{103}Pd, have also been investigated [70, 71]. While these reactions may yield higher production rates, they typically require higher incident particle energies and are associated with increased impurity formation, making them less attractive for routine medical radionuclide production.

For applications beyond brachytherapy, particularly in targeted radionuclide therapy and in vivo generator systems, the achievable specific activity of ^{103}Pd is a decisive parameter. Cyclotron-based production using the ^{103}Rh(p,n)^{103}Pd route inherently offers higher theoretical specific activity compared with reactor-based neutron capture routes, provided that efficient post-irradiation separation of palladium from the bulk rhodium target can be achieved [72].

While reactor-based production routes remain suitable for low-specific-activity applications such as brachytherapy seed fabrication, cyclotron-based production via the ^{103}Rh(p,n)^{103}Pd reaction represents the most promising pathway for generating high-purity [73], high-specific-activity ^{103}Pd for advanced radiopharmaceutical applications. Continued optimization of irradiation parameters, target design, and separation technologies is essential to enable scalable, cost-effective, and clinically compliant production of ^{103}Pd for next-generation Auger electron–based therapies.

III.5. Separation Strategies of Palladium-103 from Rhodium Targets

The separation of cyclotron- or reactor-produced ^{103}Pd from bulk rhodium targets represents one of the most challenging steps in the production of this medically relevant radionuclide. This difficulty arises primarily from the exceptional chemical inertness of rhodium, its resistance to dissolution, and the close chemical similarity between platinum-group elements. Consequently, separation strategies for ^{103}Pd have historically relied on aggressive wet-chemical methods, often involving harsh conditions, extended processing times, and substantial radioactive waste generation.

Early and widely adopted methods for isolating ^{103}Pd from irradiated rhodium targets are based on complete dissolution of the rhodium matrix, followed by selective chemical separation of palladium. Abramov et al. reported one of the classical approaches, in which irradiated rhodium was dissolved under strongly oxidizing acidic conditions, followed by multistep chemical purification to isolate palladium fractions suitable for medical use [74]. While effective, this method suffers from low rhodium recovery, high reagent consumption, and limited scalability.

Similar challenges are highlighted in systematic studies by Wang et al., who investigated separation, purification, and quality-control procedures for ^{103}Pd produced from rhodium targets [75]. Their work emphasizes that wet-chemical routes often require complex redox control, repeated precipitation or extraction steps, and careful monitoring to ensure radionuclidic and chemical purity. These processes are labor-intensive and generate considerable volumes of secondary radioactive waste.

Electrochemical dissolution has also been explored as an alternative to purely chemical dissolution. Kuznetsova et al. developed a laboratory setup

for express electrochemical dissolution of powder rhodium targets, demonstrating accelerated dissolution kinetics and improved control over the dissolution process [76]. Although electrochemical approaches reduce chemical reagent usage, they remain technically complex and are still constrained by the inherent resistance of rhodium to oxidation.

To mitigate the difficulties associated with direct rhodium dissolution, alloying pretreatments have been proposed. Ohya et al. demonstrated that alloying irradiated rhodium with bismuth prior to dissolution significantly enhances palladium separation efficiency [77]. The formation of a Rh–Bi alloy modifies the chemical behavior of rhodium, enabling faster dissolution and more selective palladium recovery. While effective, alloying pretreatments introduce additional materials into the process and require precise control to avoid contamination.

For clinical applications, particularly brachytherapy, separation strategies must meet stringent requirements for specific activity, chemical purity, and reproducibility. Afarideh et al. described the production of ^{103}Pd seeds from rhodium targets using conventional dissolution and purification techniques optimized for clinical deployment [78]. Their work underscores the trade-off between robustness and efficiency: while wet-chemical routes are well understood and regulatory-accepted, they remain resource-intensive and costly, especially given the high value of rhodium targets.

Despite decades of development, existing separation methods for ^{103}Pd from rhodium targets share several inherent limitations:

- Dependence on harsh chemical conditions to dissolve rhodium.
- Long processing times, often incompatible with high-throughput production.

- Loss of rhodium material, impacting economic sustainability.
- Generation of large volumes of radioactive waste.
- Limited flexibility for repeated irradiation–separation cycles.

These challenges have motivated the exploration of alternative, non-dissolution-based separation concepts that exploit intrinsic physical or thermodynamic differences between palladium and rhodium.

III.6. ^{103}Pd/^{103m}Rh in Vivo Generator

The concept of an in vivo radionuclide generator is based on administering a parent radionuclide that decays in situ to a therapeutically relevant daughter nuclide, ideally remaining localized at the target site defined by the carrier molecule. Such systems are particularly attractive for Auger electron therapy, where extremely short-range emissions necessitate precise spatial confinement to achieve therapeutic efficacy while minimizing off-target toxicity. Within this context, the ^{103}Pd/^{103m}Rh parent–daughter pair has been proposed as a promising in vivo generator system for targeted radionuclide therapy.

The feasibility of the ^{103}Pd/^{103m}Rh system was first evaluated from a theoretical perspective, focusing on recoil energy considerations associated with the decay process. Van Rooyen et al. demonstrated that the recoil energy imparted to ^{103m}Rh following electron capture decay of ^{103}Pd is substantially lower than that observed for α-emitting in vivo generators, such as ^{225}Ac/^{221}Fr (francium-221), and is unlikely to be sufficient on its own to rupture metal–chelator coordination bonds under ideal conditions [30]. This initial assessment suggested that the daughter nuclide could remain chelated and spatially confined, thereby supporting the viability of the system.

Subsequent investigations refined this understanding by incorporating the role of conversion electrons and Auger electron cascades. Szűcs et al. extended recoil models to include electronic after-effects of decay, demonstrating that even in β- and electron capture–decaying systems, daughter release cannot be fully excluded [79]. These studies emphasized that bond destabilization may arise not only from nuclear recoil but also from localized electronic excitation and ionization processes accompanying Auger electron emission. Similar conclusions were reached in comparative studies of the dysprosium-166 (^{166}Dy) / holmium-166 (^{166}Ho) *in vivo* generator, where electron-induced effects were shown to contribute measurably to daughter dissociation despite low recoil energies [80].

Theoretical modeling and experimental evidence indicate that the ^{103}Pd/^{103m}Rh system represents a viable in vivo generator for Auger electron therapy, while also highlighting critical challenges related to daughter retention. The combined influence of recoil, conversion electrons, and Auger-induced electronic destabilization necessitates careful selection of chelators, carrier molecules, and biological targeting strategies to mitigate unintended redistribution of ^{103m}Rh. These considerations form the foundation for the experimental investigations presented in this thesis, which aim to quantify daughter release and assess its biological implications under clinically relevant conditions.

III.7. Palladium Chelation for Radiopharmaceutical applications

The successful clinical translation of palladium-based radiopharmaceuticals critically depends on the availability of chelators capable of forming kinetically inert and thermodynamically stable complexes under physiological conditions. Palladium(II) exhibits distinct coordination

chemistry compared with many commonly used radiometals, characterized by a strong preference for square-planar geometries, rapid ligand exchange kinetics, and sensitivity to donor atom type [81, 82]. These features pose unique challenges but also offer opportunities for rational chelator design in targeted radionuclide therapy.

Investigations into palladium coordination chemistry highlighted its strong affinity for nitrogen- and sulfur-containing ligands, motivating the exploration of macrocyclic and multidentate chelators for radiopharmaceutical applications. Recent systematic studies have demonstrated that appropriately designed chelators can significantly enhance the stability of palladium complexes in biological environments. In particular, Pineau et al. demonstrated that the TE1PA chelator exhibits enhanced coordination properties toward Pd(II), yielding complexes with improved kinetic inertness and resistance to transchelation in biologically relevant media. Their work established palladium as a viable candidate for radiopharmaceutical development when paired with optimized chelation frameworks, thereby overcoming earlier concerns regarding in vivo instability [81].

Beyond classical macrocycles, alternative chelator architectures have been explored to address palladium's coordination demands. Hojorat et al. reported the relevance of oxocyclam-based chelators for Pd(II) coordination, demonstrating favorable complexation behavior and high stability in aqueous environments. Their findings underline the importance of ligand rigidity, donor atom preorganization, and electronic effects in stabilizing Pd(II) complexes suitable for radiopharmaceutical use [82]. Together with TE1PA-based systems, these studies represent a significant advance in palladium chelation chemistry tailored for nuclear medicine.

In parallel, chelator development has expanded toward functional systems designed for specific therapeutic applications. Annamalaisamy et al. reported the synthesis and biological evaluation of radioactive ^{103}Pd and ^{109}Pd bipyridyl–bisphosphonate complexes for targeted therapy of bone metastatic tumors. The bisphosphonate motif conferred strong affinity for hydroxyapatite, enabling selective accumulation in bone tissue, while maintaining sufficient complex stability for in vivo application. This work demonstrated that palladium-based radiopharmaceuticals can be successfully adapted to clinically relevant targeting strategies through appropriate ligand design [83].

Nanoparticle-based chelation strategies have also emerged as a powerful approach to overcome limitations associated with small-molecule palladium complexes. Sporer et al. developed optimized chelator and nanoparticle platforms for high-activity ^{103}Pd-loaded biodegradable brachytherapy seeds. By integrating chelation chemistry with nanostructured carriers, they achieved high radionuclide loading, enhanced retention, and controlled release profiles, highlighting the potential of hybrid chelator–nanoparticle systems for localized radionuclide therapy [84].

Complementary work by Fathy et al. further demonstrated the therapeutic relevance of palladium complexes immobilized on hydroxyapatite nanoparticles via alendronate chelation. These Pd(II)-based systems exhibited anticancer activity while benefiting from the biocompatibility and targeting properties of the nanoparticle carrier. Such approaches emphasize that palladium chelation strategies can be effectively combined with advanced drug delivery systems to improve pharmacokinetics and therapeutic indices [85].

These studies demonstrate that palladium chelation for radiopharmaceutical applications has progressed from a fundamental coordination challenge to a rapidly advancing field supported by rational ligand design, macrocyclic chemistry, and nanotechnology. The convergence of optimized chelators such as TE1PA and oxocyclam derivatives with functional targeting motifs and carrier systems provides a robust foundation for the development of ^{103}Pd-based radiopharmaceuticals. These advances are particularly relevant for Auger electron–emitting applications, where prolonged intracellular retention and minimal redistribution are essential for maximizing therapeutic efficacy while minimizing off-target toxicity.

III.8. Preclinical Studies of ^{103}Pd Auger Electron-Emitting Radiopharmaceutical

Despite the growing interest in Auger electron–emitting radionuclides for targeted radionuclide therapy, preclinical studies specifically involving palladium-103 remain extremely limited. A comprehensive search of the peer-reviewed literature, reveals no systematic in vivo preclinical therapy studies employing molecularly targeted ^{103}Pd radiopharmaceuticals comparable to those reported for other Auger emitters. This lack of experimental data represents a significant knowledge gap and underscores the exploratory nature of current research on ^{103}Pd.

In contrast to ^{103}Pd, several other Auger electron–emitting radionuclides have been extensively investigated in preclinical and in vivo settings, providing important proof-of-concept evidence for the therapeutic potential of Auger electron therapy. Early and foundational work has demonstrated that radionuclides such as iodine-125 (^{125}I) and indium-111 (^{111}In) can induce potent cytotoxicity when delivered in close proximity to

critical cellular targets, particularly the nucleus, thereby establishing key principles for Auger electron-based radiopharmaceutical design [86]. More recently, significant advances have been achieved through the development of molecularly targeted Auger emitters, including prostate-specific membrane antigen (PSMA)–directed agents, which have shown pronounced antitumor efficacy in micrometastatic prostate cancer models in vivo [87]. Parallel progress has been made in the field of DNA repair–targeted Auger electron therapy, where PARP-1–targeted Auger electron radiotheranostics have demonstrated strong preclinical efficacy, favorable tumor uptake, and highly localized DNA damage in prostate cancer models [88, 89]. Comprehensive reviews further confirm that a diverse range of Auger electron emitting radionuclides, including ^{125}I, ^{111}In, ^{67}Ga (gallium-67), and emerging metal-based systems, have reached advanced stages of preclinical evaluation, underscoring the growing maturity of Auger electron radiopharmaceutical therapy as a precision treatment modality [90, 91]. Despite this progress, palladium-103 remains notably underrepresented in preclinical studies, with very limited experimental data available on its in vivo behavior, radiobiological effectiveness, and therapeutic performance.

The absence of comprehensive preclinical studies using ^{103}Pd radiopharmaceuticals should not be interpreted as a lack of therapeutic potential, but rather as a consequence of historical limitations in radionuclide availability, separation chemistry, and suitable chelation strategies. Recent advances in ^{103}Pd production, separation, recovery, purification, and radiochemical stabilization, as addressed in the preceding sections of this thesis, now enable systematic preclinical investigation. Consequently, the present work contributes to addressing this gap by establishing the technical and radiochemical framework required for in vivo investigations and further

presents initial preclinical evaluations of ^{103}Pd-based Auger electron radiopharmaceuticals, thereby supporting their further development as candidates for targeted radionuclide therapy.

IV. Materials and methods

Rhodium metal foils (99.85% purity; 125, 25, 12, and 6 μm; Goodfellow Cambridge Ltd., Huntingdon, England) were used as cyclotron targets. Irradiations were performed using an MGC-20 cyclotron (ATOMKI, Debrecen). Activity measurements were carried out with an Atomlab™ 500 dose calibrator (Mirion Technologies, USA), and gamma spectrometry was performed with a Canberra high-purity germanium (HPGe) detector (Model 2002 CSL, USA) and Genie-2000 (V3.4.1, 2016) software. The rhodium and palladium powders were purchased from Koch-Light Laboratories Limited, UK. The deposition of palladium onto the rhodium foil was accomplished through the magnetron sputtering deposition technique using magnetron heads made by Kurt J. Lesker. The base pressure of the sputtering chamber was lower than 2×10^{-7} mbar. Circular palladium targets (purchased from Kurt J. Lesker) of 5 cm diameter were used as sputtering sources. During the layer deposition, the Argon (Ar) (99.999%) pressure (under dynamic flow) and the sputtering power were 5×10^{-3} mbar and 40 W, respectively. The sputtering rate was calculated from the layer thickness measured using an AMBIOS XP-1 profilometer. Annealing procedures were carried out using a vacuum furnace at base pressure of 7.5×10^{-7} mbar. The depth profile analysis of the samples was performed using a secondary neutral mass spectrometer (SNMS, type INA-X, produced by SPECS GmbH) in direct bombardment mode by using Ar^+ ions with low energy for sputtering (E = 350 eV) and with a current density of ~1 mA/cm^2. Post-ionized neutral particles were analyzed using a Balzers QMA 410 quadruple mass spectrometer; the erosion area was confined to a circle of 2 mm in diameter by means of a Ta mask. Surface morphology of the as-prepared and annealed samples was performed with a dual-beam scanning electron microscope from Thermo Fisher Scientific (FIB-SEM, Waltham,

MA, USA, Model: Scios 2), equipped with Bruker type Quantax Energy Dispersive X-ray system (EDS) for composition analysis.

The silicon wafer of 1 mm thickness was purchased from Crystal GmbH, Germany. The niobium foil with a thickness of 50 µm, the boron nitride (BN) ceramic, and the tungsten (W) metal disc were purchased from Goodfellow, UK. The zinc oxide (ZnO) layer (100 nm thick) was fabricated at ATOMKI via atomic layer deposition (ALD) technique in a Beneq TFS-200 reactor [92]. The ZnO layer was prepared by applying diethyl-zinc (DEZ) and water (H_2O) precursors (purchased from Sigma-Aldrich) at 100 °C reactor temperature. The consecutive pulse times were 0.3 s for DEZ followed by 10 s nitrogen purge and 0.2 s for H_2O followed by 10 s nitrogen purge. Measurements of rinsed radioactive ^{103}Pd samples were carried out using the ICP-MS Thermo Scientific X2, Waltham, MA, USA. The yttria-stabilized zirconia (YSZ) crucibles were purchased from Goodfellow Cambridge Ltd., and the alumina ceramic crucible substrates were obtained from Kurt J. Lesker Company GmbH, Fritz-Schreiter-Strasse 18, 01259 Dresden, Germany. Inductively coupled plasma mass spectrometry (ICP-MS) measurements of unirradiated (heated) rhodium foils were performed using an iCAP TQ triple quadrupole ICP-MS instrument (Thermo Fisher Scientific, Bremen, Germany), operated with Qtegra™ software for instrument control, autotuning, and data acquisition.

DOWEX® 1X8 anion-exchange resin (chloride form, 200–400 mesh) and analytical-grade reagents, including hydrochloric acid (HCl) (6 M), nitric acid (HNO_3) (65% w/w), ammonium hydroxide (NH_4OH) (28–30% w/w), ammonium acetate ($CH_3CO_2NH_4$) (0.4 M, pH 5.5), sodium acetate (CH_3COONa), ethylenediaminetetraacetic acid disodium salt dihydrate ($Na_2EDTA.2H_2O$, 0.01 M), methanol, acetone and physiological saline (0.9%

NaCl), were obtained from Sigma Aldrich–Merck, St. Louis, USA. Strata-X (polymeric, reverse-phase sorbent, 30 mg/1 mL, particle size 33 μm) and Strata-C18-E (220 mg/6 mL, particle size 55 μm) solid-phase extraction (SPE) columns were sourced from Phenomenex (Torrance, USA). DOTA-TOC (DOTA-[Tyr^3]-octreotide) was provided by Pharm-Sintez (Moscow, Russia). NOTA (1,4,7-triazacyclononane-1,4,7-triacetic acid), DOTA-TATE (DOTA-[Tyr^3]-octreotate) and gentisic acid were supplied from ABX GmbH, Radeberg, Germany. Cetuximab (Erbitux®) was obtained from Merck, AMBA peptide from Bachem AG (Bubendorf, Switzerland), and 1 micron diameter resin microspheres were made in the Helmholtz-Zentrum Dres-den-Rossendorf, Germany. All solutions were prepared using deionized water produced by a Milli-Q® purification system (Merck Millipore). Low-binding microcentrifuge tubes (Eppendorf, Germany), iTLC-SG plates (Agilent Technologies, USA), C18 mini-column chromatographic separation (Sep-Pak® C18, Waters Corporation, Milford, MA, USA), and Raytest Mini-GITA radio-TLC scanner (Raytest Isotopenmessgeräte GmbH, Straubenhardt, Germany) were used for radiochemical analyses. Radiolabeling reactions were conducted in a Thermomixer® C (Eppendorf SE, Hamburg, Germany). Centrifugation steps were performed using a benchtop centrifuge (Rotofix 32A, Hettich, Germany). NMRI nu/nu (nude) mice were obtained from Charles River Laboratories (Germany). SPECT/CT imaging and data processing employed a dedicated small animal high-resolution and high-sensitivity nanoScan® SPECT/CT instrument and a clinical PET/SPECT/CT triple modality imaging system (AnyScan TRIO system, Nucline™ acquisition software, and Fusion™ analysis software, all from Mediso Ltd., Budapest, Hungary).

IV.1. Cyclotron Irradiation of ^{103}Rh and Production of ^{103}Pd

^{103}Pd was produced via the ^{103}Rh(p,n)^{103}Pd nuclear reaction by irradiating rhodium metal foils with protons of 11 ± 0.05 MeV using a compact multiparticle cyclotron (MGC-20) at the HUN-REN Institute for Nuclear Research (ATOMKI, Debrecen). Isotope production was carried out using the cyclotron's vertical beamline system, which employs helium gas cooling on the front side of the solid target and water cooling on the back side to ensure efficient heat dissipation during irradiation [93]. The cyclotron is equipped with a newly developed and unique beam diagnostic system, namely a compact Beam Energy Monitor (BEM), which is integrated into the main beam transport channel and enables continuous, real-time monitoring of the proton beam energy across all irradiation lines, including the isotope production beamline. The measurement accuracy and performance validation of the BEM have been previously reported and described [94].

The ^{103}Rh(p,n)^{103}Pd reaction represents a well-established and widely documented cyclotron-based production route for ^{103}Pd [61], providing favorable yields at proton energies within the 8–12 MeV range [23, 95]. Rhodium foils with thicknesses of 6, 12, 25, and 125 μm were arranged in a stacked-foil configuration, from thickest to thinnest, and mounted on a copper backing plate serving as the cyclotron target holder. The assembled target stack was irradiated in multiple experimental runs to identify optimal irradiation parameters and to maximize the produced activity. The initial irradiations was performed for 2 hours (h) at a proton beam energy of 14.5 MeV and a beam current of 10 μA. Subsequent irradiations was conducted for 5.5 h using a beam energy of 10 MeV and a current of 10 μA, followed by irradiations extended to 8 h at a beam energy of 11 MeV and an increased beam current of 20 μA.

Based on these optimization experiments, a proton beam energy of 11 MeV and a beam current of 20 μA applied for a duration of 30 h were selected as the optimal irradiation conditions, taking into account rhodium foil thickness and reaction cross-section data, as illustrated in Figure 4. Under these optimized parameters, an activity of ~ 6 GBq of ^{103}Pd at end-of-bombardement (EOB) was consistently achieved for each experimental iteration.

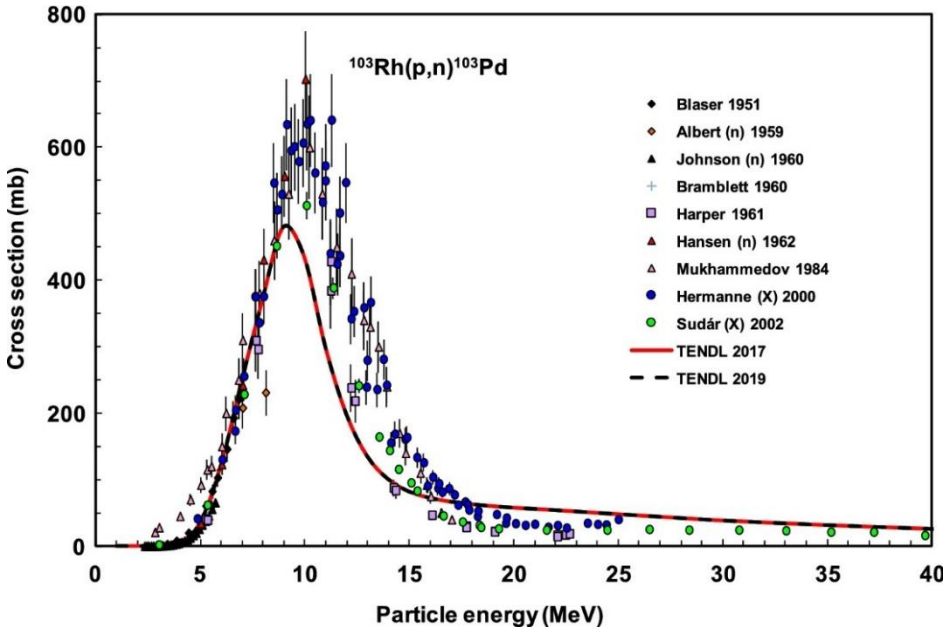

Figure 4. Experimental data and TENDL predictions for the ^{103}Rh(p,n)^{103}Pd reaction (reproduced with permission from [96]).

IV.2. Synthesis and Diffusivity Characterization of Palladium–Rhodium Alloy Samples

To estimate the intrinsic diffusion coefficient of palladium in a rhodium matrix, multilayer Pd/Rh specimens were prepared and subjected to controlled thermal annealing. Rhodium foils with a thickness of 6 μm were used as substrates and coated with a 100 nm-thick layer of natural palladium using a magnetron sputtering vapor deposition technique. This

approach enabled the formation of a well-defined Pd/Rh interface with a sharp initial concentration gradient, suitable for diffusion studies.

The prepared multilayer samples were systematically annealed under high-vacuum conditions in a general-purpose vacuum furnace at temperatures of 600 °C, 700 °C, 800 °C, and 900 °C for a fixed duration of 10 min. These annealing temperatures were selected to promote measurable interdiffusion while minimizing excessive alloying or surface degradation. The controlled thermal treatment allowed the investigation of temperature-dependent diffusion behavior within the Pd–Rh system.

Both the as-deposited and annealed samples were subsequently analyzed using secondary neutral mass spectrometry (SNMS) depth profiling. This technique provides high-resolution compositional depth profiles across multilayer interfaces and has been widely applied to diffusion and intermixing studies in sputter-deposited thin-film systems, including metallic multilayers [97]. In the present study, SNMS depth profiling enabled quantitative assessment of palladium penetration across the Pd/Rh interface and supported the determination of palladium diffusion coefficients as a function of annealing temperature.

IV.3. Design and Engineering of a Radionuclide Separation Equipment (RSE)

A dedicated radionuclide separation system (RSE) was designed, engineered, and constructed as illustrated in Figures 5 and 6 [28].

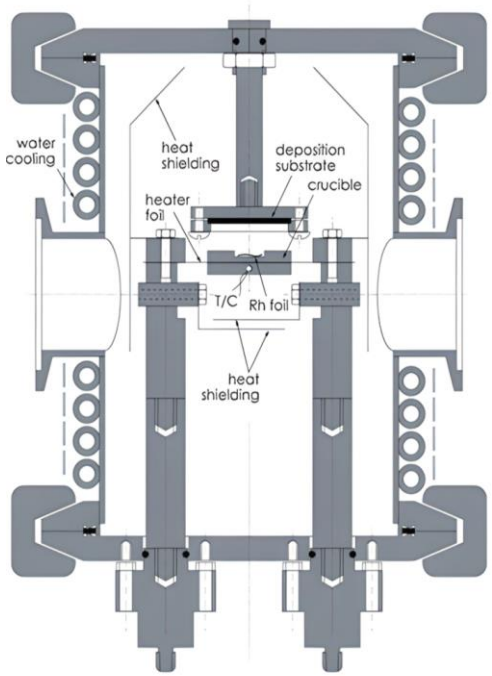

Figure 5. Conceptual schematic of the radionuclide separation equipment illustrating the main components.

Figure 6. Photograph of the preliminary radionuclide separation equipment (RSE).

The radionuclide separation equipment (RSE) operates based on a dry-distillation approach, which exploits differences in the partial vapor pressures of the target material and the resulting radioactive species. In practice, this operational principle is effective only when the radionuclide produced via irradiation exhibits a vapor pressure at least two orders of magnitude higher than that of the target material, corresponding to a minimum separation factor of approximately 100. A comparison of the vapor-pressure functions of the palladium–rhodium system demonstrates that this criterion is satisfied (Figure 7). Under these conditions, ^{103}Pd atoms are selectively volatilized from the irradiated ^{103}Rh foils and subsequently collected on a dedicated deposition substrate.

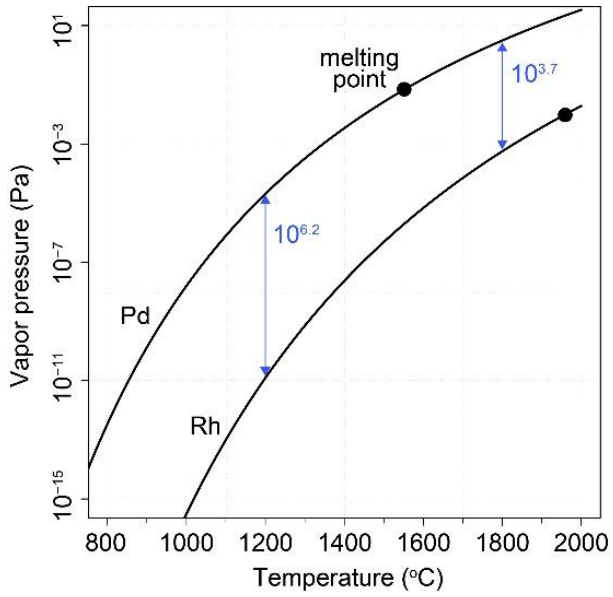

Figure 7. Partial vapor pressure of palladium and rhodium as a function of the temperature [98].

The operation of the RSE is based on resistive heating, achieved using a 50 μm-thick niobium foil cut into a tailored geometry to localize heat dissipation at the boron nitride (BN) crucible (Figure 5). The crucible

temperature was monitored using a D-type thermocouple (Re 3%W / Re 25%W), which was inserted into a dedicated hole drilled in the BN block. Heating power was supplied by a TKD-Lambda power supply (Genesys series, 180 A / 8 V).

The deposition stage consisted of the deposition substrate and a mechanical support base that maintained a fixed distance of 10 mm from the irradiated rhodium foil. For cold (non-radioactive) experiments, a silicon wafer with a thickness of 1 mm was used as the deposition substrate. In the pilot radioactive separation experiments, a 50 μm-thick niobium foil served as the deposition substrate. In subsequent separation experiments, a tungsten disc mounted on a large copper block was employed; the assembly was fixed to the top lid of the vacuum chamber and functioned as a passive heat reservoir. Given the relatively short duration of RSE operation (20 min during separation experiments employing tungsten as the substrate material), this passive cooling approach was found to be sufficient.

Pilot experiments were conducted over a temperature range of 1200–1500 °C to assess the feasibility of selective separation. In the subsequent phase, the optimal temperature conditions for efficient isolation of the two metallic elements were investigated with the aim of minimizing rhodium contamination in the deposited material. For this purpose, a test mixture consisting of equimolar amounts of rhodium and palladium powders was loaded into the RSE crucible, as illustrated in Figure 8.

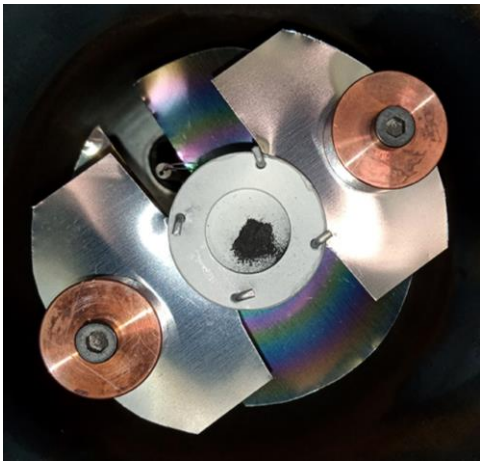

Figure 8. Overhead view of the boron nitride (BN) crucible loaded with a palladium–rhodium powder mixture.

The powder mixture was heated to 1200 °C for a duration of 10 min. The compositional purity of the palladium layer deposited on the silicon wafer substrate was subsequently examined by scanning electron microscopy (SEM) coupled with energy-dispersive X-ray spectroscopy (EDS). Following comprehensive optimization of the operational parameters and identification of the optimal temperature range for effective separation, the RSE was employed for the separation of ^{103}Pd from irradiated ^{103}Rh foils. Subsequent separation experiments were performed at a temperature of 1200 °C under high-vacuum conditions of 3–5 × 10^{-5} mbar. These parameters were selected based on theoretically optimal conditions derived from vapor pressure curves and validated through the heating separation tests conducted with palladium and rhodium powders.

Based on these experiments, which focused on optimization of the technical parameters governing the RSE design, including fine-tuning of electrical resistance, thermal conductance of electrode components, and

calibration of heating power in correlation with temperature, several functional elements of the equipment required redesign. These modifications included the implementation of thermal radiation shielding, upgrades to the cooling system, optimization of crucible material selection to avoid metallic contacts and potential alloying with the rhodium foil, and improvement of electrode contacts.

IV.4. Quantitative Measurement of ^{103}Pd Activity Using HPGe γ-Spectroscopy and an Atomlab Ionization Chamber Dose Calibrator

Quantification of ^{103}Pd radioactivity was performed using a high-purity germanium (HPGe) detector and an Atomlab ionization chamber dose calibrator. Samples subjected to activity measurements included the irradiated rhodium foils following each irradiation and separation experiment; the niobium deposition substrate after separation and subsequent hydrochloric acid treatment; the ZnO-coated tungsten disc following separation and successive treatments with hydrochloric and nitric acids; the copper-coated alumina ceramic crucible substrate after separation and nitric acid treatment; and all radioactive liquid fractions collected in vials following dissolution or extraction of ^{103}Pd from the various substrates. For HPGe measurements, gamma peak areas were corrected for background contributions and decay, and the activity of ^{103}Pd was determined using its characteristic γ-ray emission at 357.45 keV, despite its low branching ratio of 0.0221% [104]. The use of HPGe γ-spectroscopy and an ionization chamber dose calibrator enabled reliable assessment of ^{103}Pd radioactivity in all samples throughout the separation and recovery procedures.

IV.5. Improved Separation of ^{103}Pd from Irradiated ^{103}Rh via Upgraded RSE Configuration

The RSE was upgraded through the incorporation of newly designed components aimed at improving thermal stability, vacuum performance, and collection efficiency (Figure 9). In the improved configuration, the previously used collection substrate was replaced by an alumina ceramic crucible coated with a thin copper layer. This copper-coated alumina ceramic substrate proved highly effective in promoting the condensation of volatilized ^{103}Pd and significantly simplified its subsequent recovery. Active cooling was implemented by installing a water-circulation pump connected to the RSE.

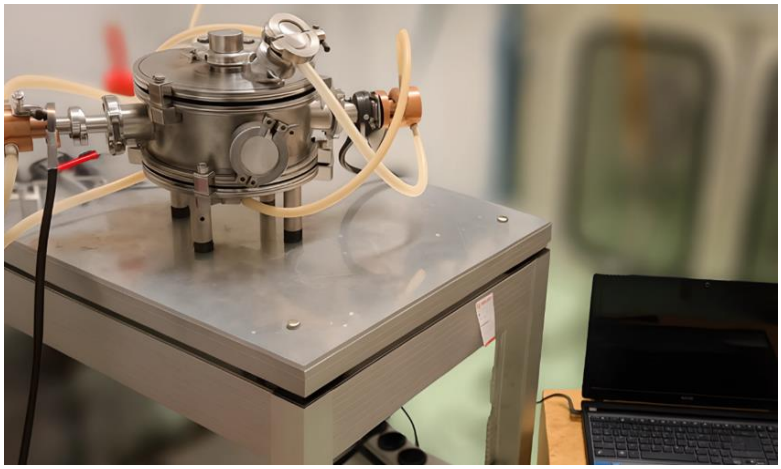

Figure 9. Upgraded, remotely controlled radionuclide separation equipment (RSE) incorporating improved components.

For each separation experiment, three irradiated rhodium foils of different thicknesses were positioned vertically inside an yttria-stabilized zirconia (YSZ) crucible, which replaced the previously used boron nitride crucible, within the RSE. This configuration was selected following a systematic evaluation of different foil arrangements and numbers to

optimize separation performance. The heating system was further upgraded to enable remote control via a newly installed PC interfaced with a TDK-Lambda Genesys 180 A / 8 V power supply. The improved system was operated at an optimized total heating power of approximately 550 W for an extended duration of 24 h, which was determined to be optimal for each separation cycle.

During operation with the upgraded RSE configuration, the crucible temperature was maintained at 1200 °C under high-vacuum conditions of 3–5 × 10^{-5} mbar. These parameters were optimized to maximize the volatilization of palladium and to ensure efficient transport and deposition of ^{103}Pd onto the copper-coated alumina ceramic collection substrate.

IV.6. Recovery and Extraction of ^{103}Pd from Deposition Surfaces

Two distinct substrate materials were employed as deposition surfaces for the collection of radioactive ^{103}Pd using the earlier RSE configuration, prior to system upgrade, as part of a systematic optimization study. In the initial experiment, a 50 μm-thick niobium (Nb) foil was used as the deposition substrate for evaporated ^{103}Pd. Following the evaporation test, the Nb foil was treated with hydrochloric acid (HCl) to recover the deposited ^{103}Pd. Different volumes of HCl and treatment durations were investigated. The resulting rinse solutions were collected in vials and subsequently subjected to quantitative analysis.

In a subsequent experiment aimed at improving the recovery efficiency of ^{103}Pd, a tungsten (W) disc with a thickness of 2 mm and a diameter of 30 mm was employed as the deposition substrate. The W disc was coated with a 100 nm-thick ZnO layer to facilitate the accumulation

of ^{103}Pd atoms. Zinc oxide was selected as a diffusion barrier to minimize penetration of ^{103}Pd into the tungsten substrate, which itself offers a high melting point and favorable chemical stability. Following deposition, the W substrate underwent sequential acidic digestion using HCl and HNO_3, following the same methodology described previously, and the resulting solutions were prepared for quantitative measurements.

Following the upgrade and optimization of the RSE, the recovery methodology was further refined. The ^{103}Pd activity deposited on the copper-coated alumina ceramic crucible substrate was recovered using an optimized acidic extraction procedure. Several extraction media and approaches were evaluated, and the most effective method involved wiping the substrate surface with cotton moistened with 0.5–1 mL of nitric acid. After recovery of the ^{103}Pd activity, the alumina ceramic crucible substrate retained its structural integrity and could be reused in subsequent separation cycles following reapplication of the copper coating (Figure 10).

(**a**) (**b**)

Figure 10. Alumina ceramic crucible substrate coated with a thin copper layer used for condensation of volatilized ^{103}Pd: (**a**) before acidic treatment; (**b**) after acidic treatment.

IV.7. Enhanced Purification of ^{103}Pd Activity

Following recovery of the ^{103}Pd activity from the alumina ceramic crucible substrate by wiping the surface with cotton moistened with 0.5–1 mL of nitric acid, the collected cotton was then immersed in 2 mL of hydrochloric acid for more than 24 h. The resulting cotton–acid mixture was subsequently filtered, and the filtrate was passed through an anion-exchange resin for purification of ^{103}Pd. After sample loading, the column was sequentially washed with hydrochloric acid and water to remove residual impurities, and purified ^{103}Pd was eluted using 1 mL of ammonium hydroxide. This eluent was selected based on prior optimization studies, in which ammonium hydroxide consistently provided the highest recovery and selectivity for ^{103}Pd.

The purified ^{103}Pd solution was subsequently heated to remove residual ammonia and reconstituted in 500 μL of 0.05 M HCl to obtain the final radiochemically pure ^{103}Pd. Thereafter, the successfully produced, separated, and purified ^{103}Pd activity from two independent experimental batches was transported to Semmelweis University in Budapest by a licensed radiopharmaceutical transport service for in vivo applications and preclinical studies (Figure 11).

(**a**) (**b**)

Figure 11. Photographs of the certified transport containers used for the shipment of purified ^{103}Pd activity from ATOMKI (Debrecen) to Semmelweis University (Budapest) for preclinical studies: (**a**) first transport batch; (**b**) second transport batch.

IV.8. Separation of Cold Palladium from Unirradiated Rhodium Foils for ICP-MS Analysis

Using the upgraded RSE setup, three unirradiated rhodium foils with a thickness of 6 μm were subjected to a heating treatment to evaluate their residual (cold) palladium content by ICP-MS. For comparison, three additional rhodium foils of identical thickness were kept untreated (unheated). This experimental approach was designed both to assess the effectiveness of cold palladium removal from the rhodium matrix and to reduce residual palladium content prior to irradiation, thereby maximizing the specific activity of the subsequently produced ^{103}Pd.

The rhodium foils were positioned vertically inside the yttria-stabilized zirconia (YSZ) crucible within the RSE and heated for a duration of 24 h. During the heating process, the system was operated at an applied power of approximately 550 W, corresponding to a crucible

temperature of around 1200 °C under high-vacuum conditions of 3–5 × 10^{-5} mbar.

Cold palladium volatilized from the heated rhodium foils and deposited onto the copper-coated alumina ceramic crucible substrate. The deposited palladium was recovered by wiping the substrate surface with cotton moistened with 0.5–1 mL of nitric acid. The resulting solution was collected for ICP-MS analysis. A control sample was prepared in parallel using the same recovery procedure applied to a clean alumina ceramic crucible substrate without copper coating. These solutions, together with samples obtained from the heated (treated) and untreated (unheated) rhodium foils, were analyzed by ICP-MS to quantify palladium content and to evaluate the effectiveness of the cold palladium removal process.

IV.9. Radiolabeling of ^{103}Pd with the DOTA-TOC Chelator for the Evaluation of ^{103m}Rh Daughter Nuclide Release

The purified ^{103}Pd-radionuclide was complexed with 10^{-3} M DOTA-TOC strong peptide-chelator bio-conjugate chelator, dissolved in 0.4 M ammonium acetate buffer (pH 5.5), by incubation in a thermomixer for 1 h at 90 °C. The resulting [^{103}Pd]Pd–DOTA-TOC complex was immobilized onto the stationary phase of a Strata-X SPE (reverse-phase column) and a Strata-C18 hydrophobic column. The columns were then washed repeatedly with 0.01 M EDTA to remove unbound chelating agents and possible free metal ions, ensuring that only the chelator-bound ^{103}Pd–complex remained retained. The overall preparation procedure is illustrated in Figure 12.

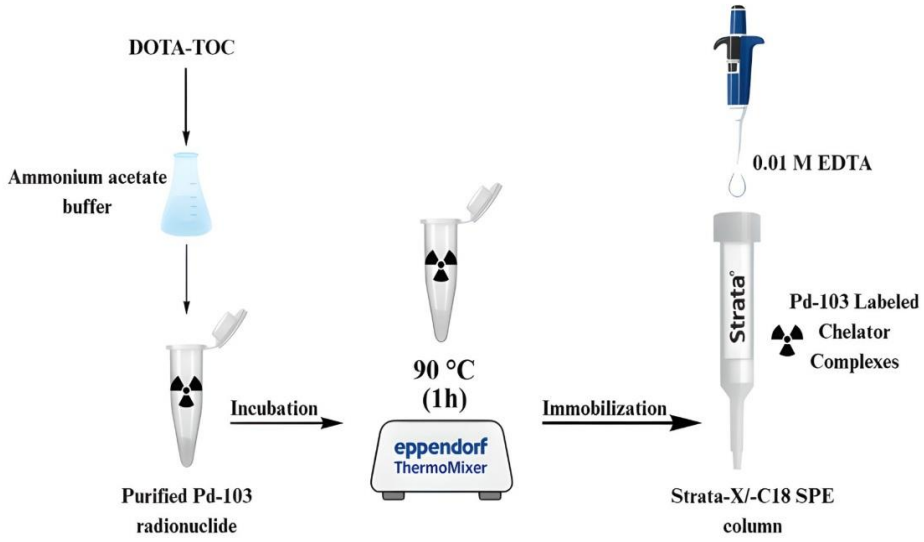

Figure 12. Experimental protocol for the preparation of [^{103}Pd]Pd–DOTA-TOC complexes.

The elution and washing procedure itself served as an effective quality-control step. The solid-phase extraction columns used are selective for retaining the chelator-bound complexes; therefore, only Pd complexes stably coordinated to the chelator remain immobilized on the column. Any unbound or weakly bound Pd species would be removed during the washing steps and detected in the eluates. Consequently, the activity measured on the column after washing corresponds exclusively to chelator-complexed Pd, confirming the chemical identity and stability of the Pd complexes under the applied experimental conditions.

IV.10. Experimental Evaluation of ^{103m}Rh Daughter Nuclide Release from ^{103}Pd-Radiolabeled Complexes

The [^{103}Pd]Pd–DOTA-TOC–loaded Strata-X column was eluted daily with 0.8 mL of 0.01 M EDTA over four consecutive days at 24 h intervals. In parallel, the [^{103}Pd]Pd–DOTA-TOC–loaded Strata-C18

column was eluted daily with 5 mL of 0.01 M EDTA over the same duration and at identical intervals. The procedure was repeated to enable statistical evaluation of ^{103m}Rh daughter radionuclide release. The larger elution volume applied to the Strata-C18 column reflected its approximately fourfold greater packing size compared with the Strata-X column. Radioactivity in both Strata-X and Strata-C18 columns was measured before and after each elution, as well as in the collected eluates, using gamma spectroscopy to quantify radionuclide release.

The C18 column used in this study selectively bind the peptide component and do not retain EDTA or free metal ions; consequently, EDTA is not retained on the column. Owing to the low kinetic inertness and high thermodynamic stability of EDTA–metal complexes, EDTA efficiently complexes free metal ions and facilitates their removal from the column. The excess EDTA therefore removes unbound metal ions resulting from post-decay effects, and the measured decrease in column activity corresponds to the loss of the daughter radionuclide.

The eluted activity was attributed to the release of free ^{103m}Rh daughter nuclides from the chelator as a consequence of Auger electron–induced ionization. The ^{103m}Rh isotope was identified and characterized by its diagnostic X-ray emission at 39.76 keV (0.068% intensity). Gamma emissions were measured using a Canberra HPGe detector, and spectra were analyzed using Genie software. Decay corrections were applied to the activities measured in the eluates and remaining on the columns relative to the initial activity at the time of column preparation.

Due to the low intensity of the characteristic X-ray emission, absolute activity quantification was not feasible because of self-absorption

effects and non-ideal measurement geometry associated with liquid samples. However, as the study focused on activity ratios, the use of identical glassware, equipment, measurement geometry, and counting times ensured reliable relative quantification. The procedure used to evaluate ^{103m}Rh release is illustrated in Figure 13.

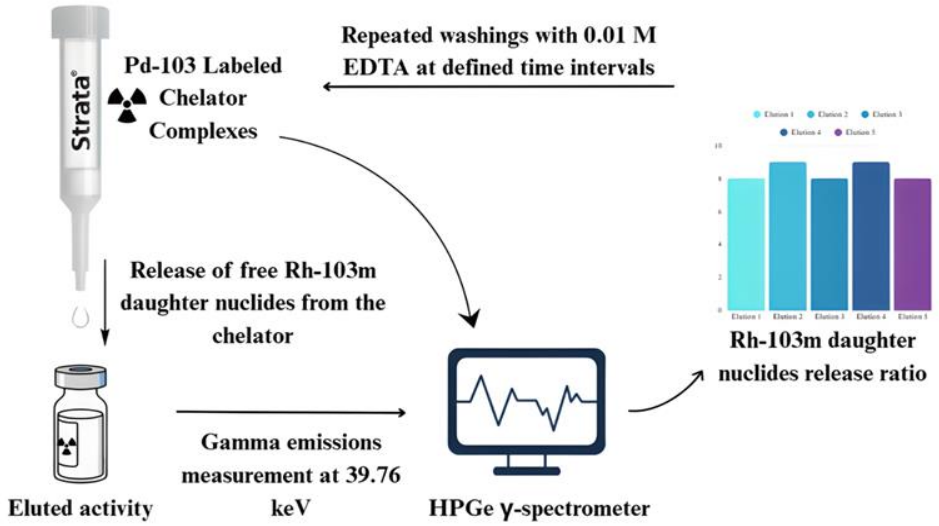

Figure 13. Quantification procedure for ^{103m}Rh-daughter nuclides released from [^{103}Pd]Pd–DOTA-TOC complexes.

IV.11. Radiolabeling of ^{103}Pd with NOTA and DOTA-TATE Chelators for In Vivo Applications

IV.11.1. Radiolabeling of [^{103}Pd]Pd–NOTA and Conjugation with Biomolecules

For radiolabeling, the purified [^{103}Pd]$PdCl_2$ solution (≤100 µL per reaction) was mixed with the NOTA-bioconjugate, either dissolved or suspended (for microspheres), in 100 µL of 0.1 M acetate buffer at pH 5.5, resulting in a final reaction volume of 200 µL. The mixture was incubated

in a thermomixer (500 rpm) at 95 °C for 20 minutes to facilitate chelation, after which the mixture was briefly centrifuged and allowed to cool to room temperature. After cooling to room temperature, radiochemical yield was assessed by C18 mini-column chromatographic separation and instant thin-layer chromatography (iTLC) using 1 M ammonium acetate and methanol as the mobile phase (Figure 14). Prior to administration, the radiolabeled solution was diluted with physiological saline to the required volume and activity concentration.

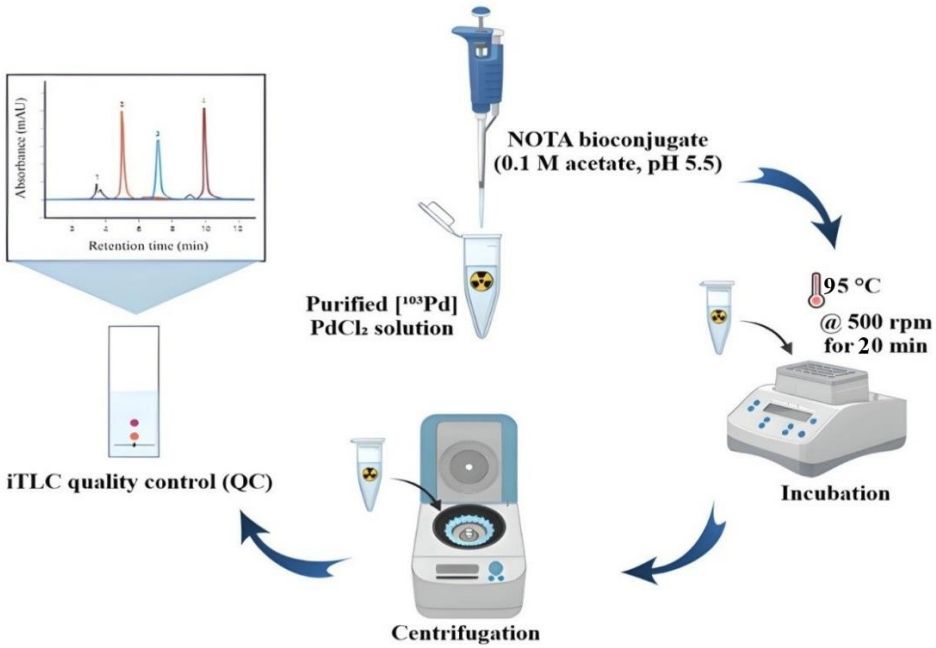

Figure 14. Radiolabeling protocol for the preparation of [^{103}Pd]Pd–NOTA bioconjugates and radio-chemical quality control.

Using this approach, the following biomolecules were successfully functionalized with NOTA and radiolabeled with ^{103}Pd: (i) Macroaggregated Serum Albumin (MAA) particles, for lung-targeted deposition studies; (ii) AMBA, a bombesin analogue; (iii) resin

microspheres for lung-targeted deposition studies; and (iv) cetuximab, a clinically relevant monoclonal antibody targeting the epidermal growth factor receptor (EGFR) [99].

IV.11.2. Radiolabeling of [^{103}Pd]Pd–DOTA-TATE

Radiolabeling of the purified ^{103}Pd with the DOTA-TATE (DOTA-[Tyr^3]-octreotate) peptide was performed using a standardized metal-ion complexation protocol adapted from established procedures [100]. The DOTA-TATE peptide was supplied in lyophilized form and reconstituted in sodium acetate buffer prior to use.

For radiolabeling, 4 mg of gentisic acid (radioprotectant) were dissolved in 0.8 mL of 0.4 M sodium acetate (NaOAc) buffer. Subsequently, a palladium-103 chloride solution containing 712 MBq of activity in 0.68 mL was added to the buffered gentisic acid solution. Thereafter, 40 μg of DOTA-TATE peptide were introduced into the reaction mixture. The resulting solution was incubated at 95 °C for 25 min to promote complex formation. After incubation, the vial was briefly centrifuged (10 s) and allowed to cool to room temperature prior to quality control analysis.

IV.12. Administration and Imaging Protocol of [^{103}Pd]Pd–NOTA in Murine Models

NMRI Nu/Nu mice were used for the imaging studies. Animals received an intravenous injection of 100 μL of [^{103}Pd]Pd–NOTA, corresponding to cca. 60 MBq per mouse. SPECT/CT acquisitions were performed at multiple time points following tracer administration. All imaging procedures were conducted under isoflurane anesthesia; which

was maintained using 1.5–2% isoflurane in medical oxygen, adjusted according to the animal's respiration rate.

Imaging was performed using a dedicated small animal high-resolution and high-sensitivity nanoScan® SPECT/CT instrument equipped with multi-pinhole collimators (Figure 15). For ^{103}Pd, a high-energy tungsten collimator (aperture 65), recommended by the manufacturer for isotopes with gamma emissions above 250 keV, was applied.

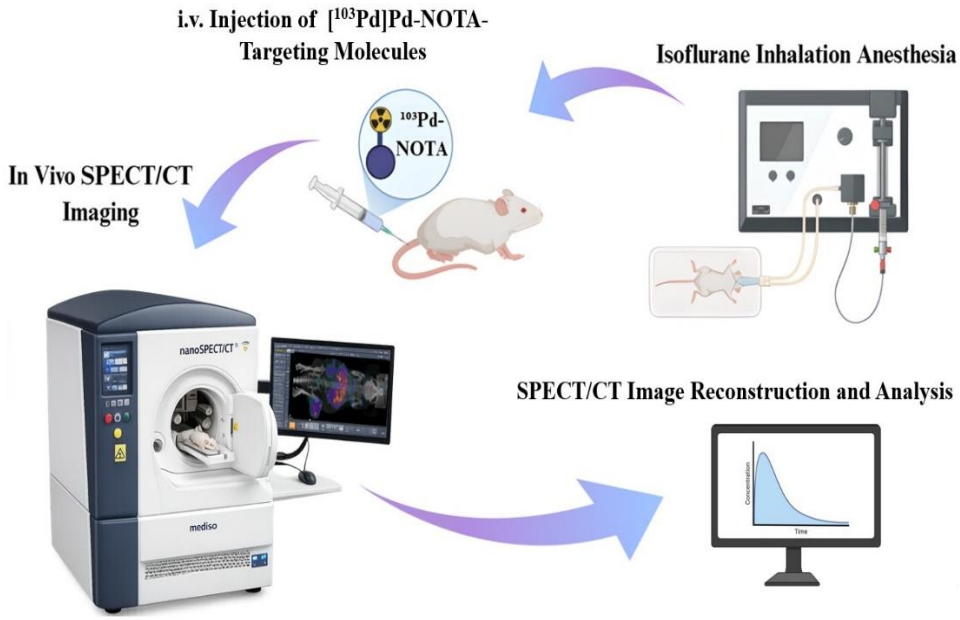

Figure 15. Experimental Workflow for [^{103}Pd]Pd–NOTA Administration and nanoSPECT/CT Imaging in Murine Models.

Gamma-ray emissions and their relative abundances were processed using the Nucline acquisition software (Mediso Ltd., Budapest, Hungary) as summarized in Table 1. Of the three detectable emissions of ^{103}Pd, only the primary 20.5 keV peak was used for SPECT image

acquisition, applying a 20% energy window centered on this peak. However, due to the presence of high-energy peaks, high stopping-power collimators were required to suppress beam-related artifacts.

Table 1. Detectable gamma emissions and corresponding relative abundances of ^{103}Pd used for SPECT imaging.

Name	Peak (keV)	Intensity (%)
Primary	20.50	76.930
Secondary	39.75	0.068
Tertiary	357.45	0.022

Whole-body SPECT/CT imaging was performed using 30 frames per cycle with a termination condition of 120 s per frame, covering a longitudinal scan range of 128 mm. SPECT data were reconstructed using 0.2 mm isovoxels. Co-registered X-ray CT images were acquired using a 55 kV source voltage in cone-beam spiral mode system with a pitch of 2.5. Semi-quantitative analysis of SPECT data was performed by measuring counts per unit volume (counts/mL). Image processing and analysis were performed using the Fusion software package (Mediso Ltd., Budapest, Hungary).

IV.13. Administration and Imaging Protocol of [^{103}Pd]Pd–DOTA-TATE in a Canine Model of Spontaneous Liver Cancer

Use of a naturally occurring canine malignancy provides a clinically relevant intermediate model bridging rodent studies and potential human applications. All procedures were conducted with the owner's consent and in accordance with institutional veterinary ethical

guidelines. A 12.5-year-old female Hungarian Vizsla family dog was diagnosed with a histologically confirmed, spontaneous, and metastatic late-stage insulinoma exhibiting somatostatin receptor subtype-2 (SSTR2) expression, was included as a translational large-animal model for imaging and therapeutic investigation (Figure 16). The dog received an intravenous administration of approximately 500 MBq of [^{103}Pd]Pd–DOTA-TATE solution diluted with physiological saline in a total injection volume of 2 mL. Thereafter, continuous veterinary monitoring was performed, including regular assessment of blood glucose levels to detect episodes of hypo- or hyperglycaemia. A trial acquisition of SPECT/CT imaging data was subsequently performed at 1 h post-injection to monitor tracer biodistribution and tumor uptake over time. Notably, no anesthesia was required during image acquisition, as the animal remained fully calm and cooperative throughout the scanning procedures.

Imaging trials aimed at detecting radioactive signals originating from the injected palladium activity were conducted at the Semmelweis Clinic of Medical Imaging (Budapest, Hungary) using a PET/SPECT/CT trimodality system (AnyScan TRIO, Mediso Ltd., Hungary). For ^{103}Pd, all relevant photon emissions listed in Table 1 were considered for image acquisition. SPECT/CT imaging was performed using a 20% energy window, including the tertiary 357.45 keV gamma emission, to maximize detection sensitivity while maintaining adequate energy discrimination.

Figure 16. Canine model during SPECT/CT imaging with [^{103}Pd]Pd–DOTA-TATE.

All animal experiments were conducted in accordance with the ARRIVE guidelines and the 3R principles. The studies were approved by the local and national animal welfare authority, the Pest County Government Office, under registration number PE/EA/00929-5/2021 for the rodent experiments and under the same registration number for the canine studies. Approval for the canine study additionally included the full informed consent and written, signed authorization of the dog's owner.

V. Results

V.1. Optimized Production of ^{103}Pd

After multiple irradiations, 11 MeV was identified as the optimal proton energy for ^{103}Pd production. This energy lies near the peak of the ^{103}Rh(p,n)^{103}Pd excitation function and provides a favorable compromise between production yield and radionuclidic purity. Operation at 11 MeV achieves high cross-section for the desired ^{103}Rh(p,n) channel while remaining below the thresholds of competing side reactions such as ^{nat}Rh(p,pn)$^{102/102m}$Rh and ^{nat}Rh(p,p2n)$^{101/101m}$Rh. These side nuclear reactions generate long-lived impurities (^{101m}Rh, ^{101}Rh, ^{102m}Rh, ^{102}Rh) that degrade the radionuclidic purity. The excitation function data reported by Tárkányi et al. [96] (Figures 17 and 18), together with our experimental evaluations, clearly demonstrate that restricting the beam energy to approximately 11 MeV ensures efficient ^{103}Pd generation while significantly suppressing formation of these undesirable radionuclidic by-products.

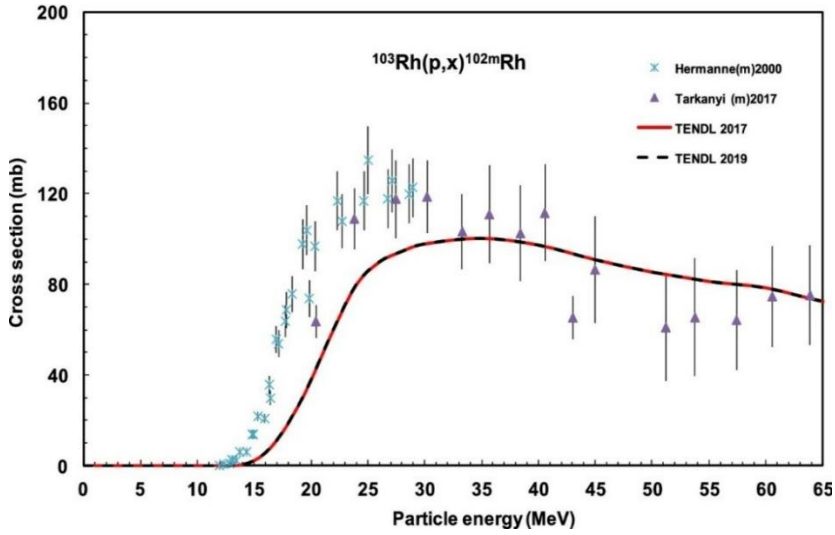

Figure 17. Experimental excitation-function data compared with TENDL-predicted cross-sections for the ^{103}Rh(p,x)^{102m}Rh reaction. (Reproduced with permission from [96].)

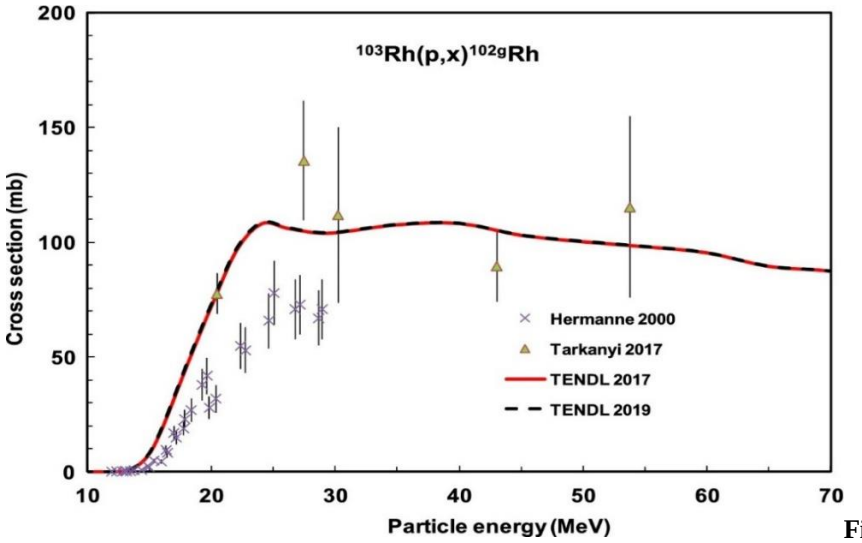

Figure 18. Experimental excitation-function data compared with TENDL-predicted cross-sections for the the ^{103}Rh(p,x)^{102g}Rh reaction. (Reproduced with permission from [96].)

To verify the radionuclidic purity of the produced ^{103}Pd and to confirm the minimization of side nuclear reactions at a proton energy of

11 MeV, post-irradiation γ-spectral analysis was performed using HPGe γ-spectroscopy. The detected γ-lines were evaluated against known decay schemes of ^{103}Pd/^{103m}Rh and potential rhodium contaminants. The identified γ-emissions and their corresponding intensities are summarized in Table 2.

Table 2. Post-irradiation γ-spectral analysis of ^{103}Pd/^{103m}Rh and evaluation of potential Rh radionuclidic contaminants produced at 11 MeV proton irradiation.

	Energy (keV)	Intensity (%)	Identified
^{103}Pd / ^{103m}Rh decay products	39,7	0,0683	Yes (Evaluated)
	53.3	3×10^{-5}	No
	62.4	0.00104	Yes
	241.9	5×10^{-7}	No
			Yes
	295,0	0,00280	No
	317,7	$1{,}50 \times 10^{-5}$	Yes (Evaluated)
	357,5	0,0221	No
	443,8	$1{,}50 \times 10^{-5}$	Yes
	497,1	0,00396	
Possible ^{102}Rh / ^{102m}Rh contaminants	475.1	46	No
	475.1	95	No
Possible ^{101}Rh / ^{101m}Rh contaminants	198,0	73	No
	306,9	81	No

V.2. Characterization of Elemental Interdiffusion at the Palladium–Rhodium Interface

The most critical factors that determine the feasibility of the dry distillation technique are the advantageous relative vapor pressure of palladium and rhodium, and the diffusion coefficient of palladium in the rhodium matrix. The latter quantity was examined in specific multi-layer samples comprising a palladium–rhodium interface, which were annealed at different temperatures from 600 to 900 °C. The interdiffusion rates in the annealed samples were analyzed via depth profiling measurements using the secondary neutral mass spectrometry (SNMS) technique. The equipment was operated in direct bombardment mode by using Ar^+ ions with a low energy for sputtering (E = 350 eV) and with a current density of ~1 mA/cm^2. The erosion area was confined to a circle of 2 mm in diameter by means of a Ta mask. The lateral homogeneity of the ion bombardment was checked by a profilometer (Ambios Technology Inc., USA, Santa Cruz, CA, Model: XP-I) to analyze the depth of the crater sputtered and to convert the sputtering time to depth scale.

Our findings revealed a noteworthy degree of elemental interdiffusion between the two constituents, as shown in Figure 19, yielding valuable insights for the formulation of subsequent systematic measurements. The obtained depth profile exhibited characteristics indicative of an ideal depth profile; however, at more advanced stages of the diffusion process (> 700 °C), a long tail emerges that can be attributed to the effect of surface roughness. Indeed, the etching speed of Ar^+ ions may sensitively depend on the surface morphology, referring to the common experience, that peaks are eroded faster than valleys, eventually leading to a distorted reconstruction of depth profiles. An ab initio simulation of the etching process has been carried out. We assumed a

model function for the etching speed describing its dependence on the local morphology of the surface, aligning with common observations that peaks undergo erosion at a faster rate than valleys. Figure 19d illustrates the least-square fit of the model (green curve), which is compared to the depth profile of uniform etching (blue curve) with the same diffusion coefficient used as a single parameter. The surface quality may critically affect the accuracy of the deduced diffusion coefficient.

Upon annealing at 600 °C, a discernible accumulation of rhodium at the surface was evident, suggesting the plausibility of rhodium diffusion through the palladium layer via a grain boundary diffusion mechanism [101], which occurred at a faster rate than the diffusion of palladium into the rhodium foil. Subsequent annealing at higher temperatures further substantiated this phenomenon, revealing a temperature-dependent increase in rhodium content within the palladium layer. Ultimately, this led to the attainment of a palladium layer fully impregnated with rhodium, coinciding with the concurrent diffusion of palladium into the rhodium foil.

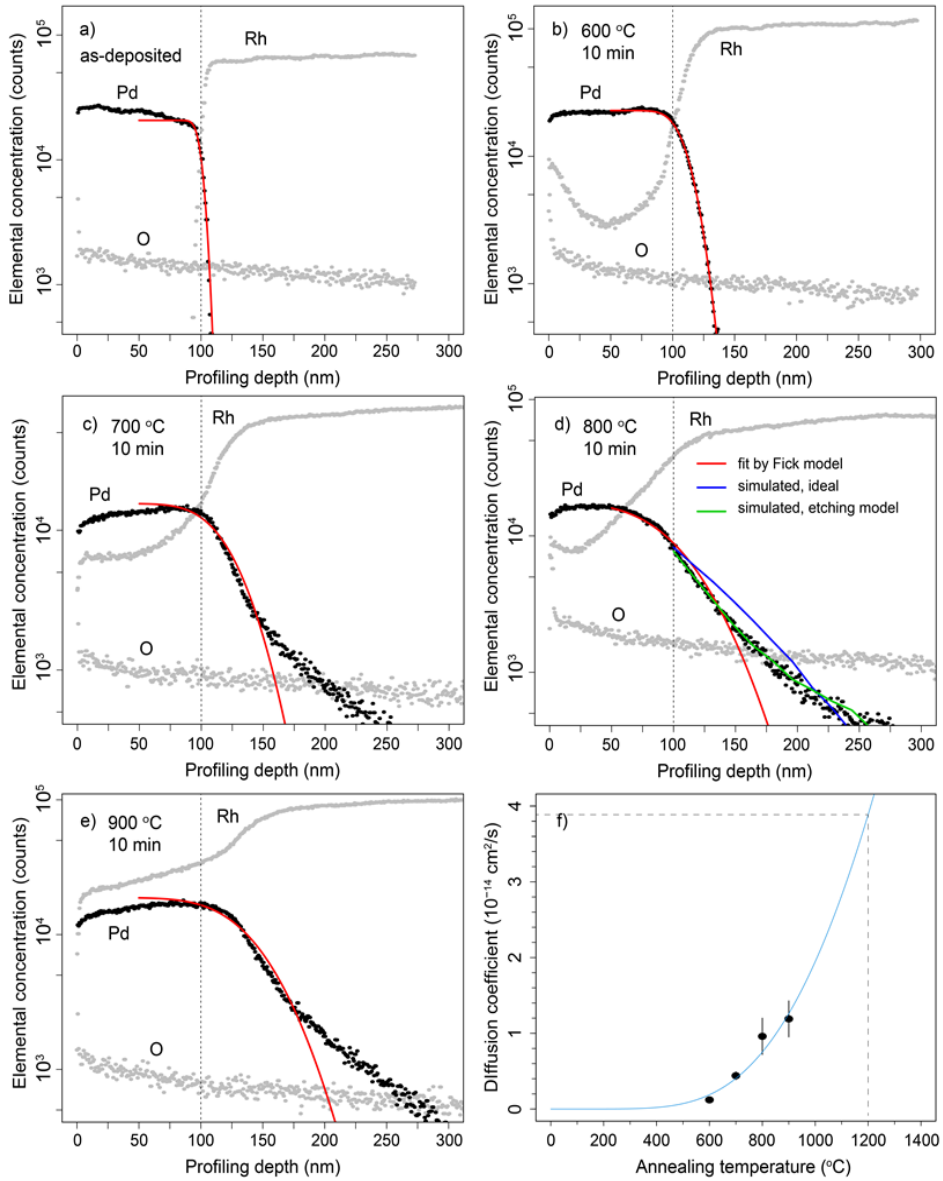

Figure 19. SNMS depth profiling analysis for: (**a**) the control sample; (**b**) the annealed sample at 600 °C for 10 min; (**c**) the annealed sample at 700 °C for 10 min; (**d**) the annealed sample at 800 °C for 10 min; (**e**) the annealed sample at 900 °C for 10 min; and (**f**) Palladium-in-rhodium diffusion coefficient deduced by fitting palladium profiles plotted as a function of the annealing temperature. The fit (blue curve) results in an activation energy of palladium displacement of 0.55 eV. The extrapolated value of ~ 4 × 10^{-14} cm^2/s is calculated for 1200 °C, the temperature at which the separation experiment was carried out.

A preliminary value for the lattice diffusion constant of the palladium-in-rhodium matrix at the annealing temperatures could be obtained, yielding 0.2–1.5 × 10^{-14} cm^2/s, by fitting the palladium concentration profiles with the formulation of Fick's second law [102, 103]:

$$N = N_0 \operatorname{erfc}\left(\frac{x}{2\sqrt{Dt}}\right), \quad (1)$$

Where x is the penetration depth of palladium atoms, D is the diffusion coefficient, and t is the annealing time. By fitting the obtained values with the Arrhenius equation, an activation energy of $E_A = 0.55$ eV was obtained:

$$D = D_0\left(-\frac{E_A}{RT}\right). \quad (2)$$

An approximate value of $D = 4 \times 10^{-14}$ cm^2/s for the diffusion coefficient was also deduced via extrapolation to 1200 °C, which is still a moderate value that can be practically relevant only for thin layers and the minute-scale operation of the equipment. However, a systematic measurement of depth profiles over a wider temperature range and interdiffusion corrections would be needed for the accurate determination of absolute extraction rates.

V.3. EDS Purity Analysis of Separated Non-Radioactive Palladium

To verify the separation power of the dry distillation method proposed for ^{103}Pd, an evaporation probe was performed, with a powder mixture of natural (non-radioactive) palladium and rhodium with a 1:1

stoichiometric ratio. The substrate used for probing the deposition was a silicon wafer of 1 mm thickness. The evaporation test was performed at 1200 °C for 10 min. The compositional purity of the deposited palladium layer was examined via scanning electron microscopy (SEM) using energy-dispersive X-ray spectroscopy (EDS). The analysis of the EDS spectrum resulted in a Rh decontamination factor greater than 100, estimated from the observed absence of rhodium content at the expected location, considering the detection limit of 0.1 at% specified for the spectrometer (Figure 20).

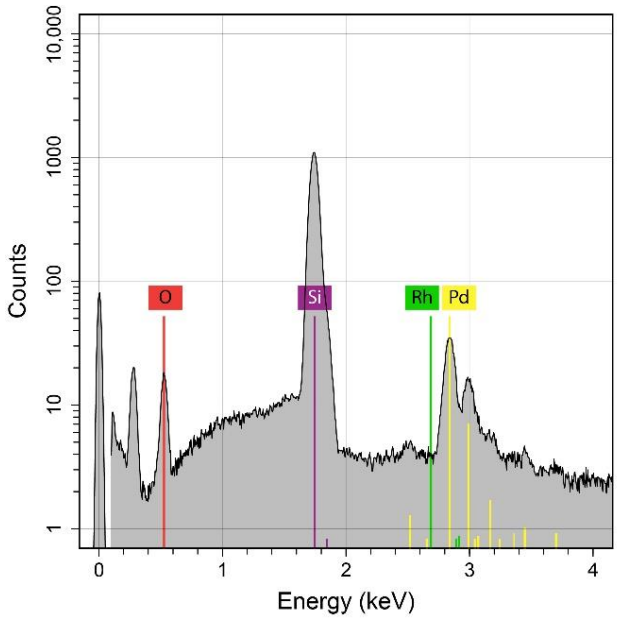

Figure 20. Elemental composition of the deposited layer on a silicon substrate examined via EDS.

The initial mass of the powder mixture was measured as 29 mg, while, after the heating process, the remaining material was 23 mg. Assuming a negligible evaporation rate for the rhodium, the evaporated palladium was calculated to be 6 mg, indicating that the separation power

and material purity are satisfactory even at a moderate operational temperature (1200 °C).

V.4. Separation Efficiency of ^{103}Pd

The irradiated rhodium foil was heated up in the RSE to evaporate and deposit the ^{103}Pd onto the substrate via distillation. The evaporation efficiency of the palladium-in-rhodium matrix was also investigated with a random-walk simulation, which described the dependence of evaporation rates on the process time and film thickness, as well as the diffusion coefficient. The simulated evaporation efficiencies are plotted in Figure 21 as a function of the process time. The simulation determines the moment when particles escape from the foil, reaching either of the two surfaces. Within a specified process time, the fraction of escaped particles relative to the initial number of particles is determined and given as the term evaporation efficiency. Fitting this evaporation efficiency to the experimental value of 14% obtained in the separation experiment using the earlier RSE configuration and the ZnO/W disc at 20 min of heating, we could determine a diffusion coefficient approximately two orders of magnitude higher than the one determined from the depth-profiling analysis. A potential explanation for this discrepancy may be related to the oversimplified model of the random-walk diffusion, which used a constant time step of $\Delta t = 1\mu s$ and a displacement element $\Delta x = \sqrt{2D\Delta t}$, additionally, it did not account for contributions stemming from atomic migration on grain boundaries, temperature-dependent displacement energy, or the diffusion of rhodium atoms to the opposite direction.

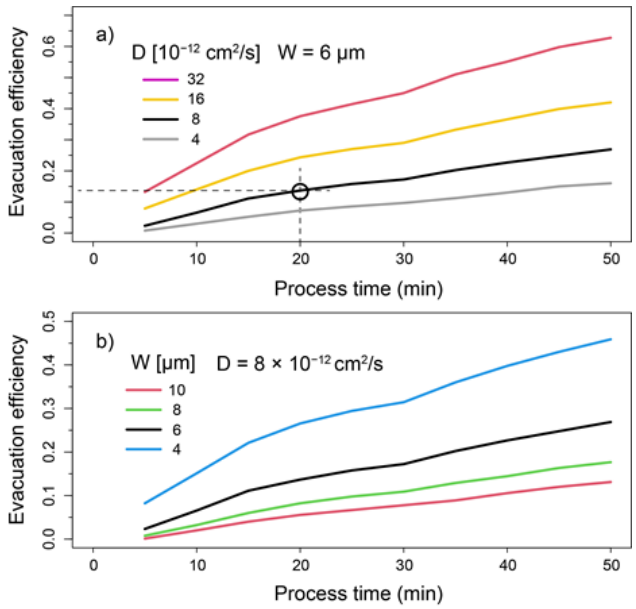

Figure 21. Simulated evacuation efficiency as the ratio of emitted ^{103}Pd with respect to the total amount in the rhodium foil. The evacuation efficiency is plotted at varying: (**a**) diffusion coefficients *D*; (**b**) foil thicknesses (W). The measured ratio of evaporated-to-produced ^{103}Pd is also provided (open circle).

In that separation experiment, the measured activity on the ZnO/W substrate was 25% of the missing activity in the rhodium target. Calculating the solid angle of the deposition substrate viewed by the target foil, we obtained 2.75 sr, which can be converted to a coverage of 22%. This value agrees well with the measured ratio of activity deposition.

Despite the low development level of the earlier RSE configuration, a considerable amount of ^{103}Pd activity was separated without rhodium contamination. The RSE design later incorporated accurate temperature control, thermal shielding, a cooling system, and improved electric contacts. The separation experiment was then repeated using a ZnO-covered W disc as the deposition substrate. The parameters and processing efficiencies obtained in the two experiments that used

niobium and ZnO-covered W disc substrates are detailed in Table 3. The ZnO layer was hypothesized to accumulate the ^{103}Pd and prevent its burial within the W substrate. The comparison of the two experiments apparently showed a higher separation efficiency when the Nb substrate was used; however, both cases confirm the applicability of the proposed technique.

Table 3. Measured activities and processing efficiency in ^{103}Pd separation.

	Substrate	T_{evap}	Δt_{evap}	EOB	Evaporated		Deposited	
		°C	min	MBq	MBq	$\%_{EOB}$	MBq	$\%_{evap}$
Pilot experiment	Nb foil	~1500	10	7.87	3.54	45	1.49	42
Separation experiment	ZnO/W disc	1200	20	31.9	4.47	14	1.12	25

Two principal issues were identified during the pilot experiments and required reconsideration in order to maximize palladium evaporation efficiency. The first concerned the thickness of the rhodium target foil, which was set to 6 μm in the pilot studies. While this thickness proved adequate for producing measurable amounts of radioactivity during short irradiation times of a few hours, and sufficiently thin to allow emission of a substantial fraction of the produced ^{103}Pd, it is not optimal from the standpoint of nuclear reaction yield. Thicker rhodium foils, on the order of ~100 μm, would be better matched to the broad cross-section maximum of the ^{103}Rh(p,n)^{103}Pd reaction and could therefore enable the production of higher-activity batches. However, evaporation rates governed by diffusion processes are inherently less favorable in thicker layers. This limitation may be partially mitigated by extending the separation duration,

allowing diffusion-driven palladium transport to compensate for the reduced evaporation rate. Thus, the 6 µm foil represented a practical compromise in the pilot experiments, balancing sufficient activity production with efficient palladium release under short irradiation and separation conditions.

The second concern was related to deposition efficiency and the selection of an appropriate deposition substrate compatible with subsequent dissolution and recovery steps. Because the deposition surface is heated by thermal radiation from the crucible, elevated temperatures enhance diffusion of deposited ^{103}Pd into the substrate material. This process increases the fraction of palladium buried beneath the surface and renders it inaccessible even under aggressive acidic digestion conditions. In the earlier RSE configuration, the deposition substrate was initially a polished niobium foil without surface modification and was later replaced by a tungsten disc coated with a ZnO layer. The ZnO coating was intended to promote surface accumulation of ^{103}Pd, inhibit diffusion into the tungsten bulk, and provide a substrate compatible with both high-temperature operation and acidic dissolution.

The operational parameters of the separation equipment were systematically examined in relation to the extraction efficiency of ^{103}Pd. Based on palladium–rhodium interdiffusion measurements, it was determined that significant palladium extraction rates can be achieved at temperatures well below the melting point of palladium (1552 °C), specifically at an operating temperature of 1200 °C with a separation duration of 24 h.

The separation of ^{103}Pd from irradiated ^{103}Rh foils using the improved and upgraded RSE configuration resulted in yields ranging from 64% to 86% (Table 4).

Table 4. Summary of ^{103}Pd separation yields under different experimental conditions.

	Substrate	T_{evap}	Δt_{evap}	Foil Thickness	Separation Yield (%)			
		°C	h	µm	Run 1	Run 2	Run 3	Run 4
Improved separation experiments	Alumina	1200	24	12/12/6	74	83	64	86

These values demonstrate the high efficiency of the diffusion-driven release and dry-distillation–based collection approach, representing a robust alternative to conventional wet-chemistry procedures. Traditional chemical dissolution and separation methods have been reported to suffer from lower overall ^{103}Pd recovery and activity losses due to multi-step processing and incomplete chemical separation [27].

In contrast, the upgraded RSE, incorporating enhanced thermal control, improved vacuum stability, and an optimized copper-coated Alumina ceramic crucible collection substrate, achieved significantly higher yields of ^{103}Pd separation than the earlier RSE configuration [28]. This improvement of more than ~50% clearly confirms the superior performance of the upgraded system. Moreover, the enhanced RSE enables scalable processing while reducing reagent consumption, minimizing radioactive waste generation, and lowering overall operational complexity.

Moreover, after each dry-distillation cycle, the irradiated ^{103}Rh foils were found to retain their mechanical integrity, mass, and surface morphology, indicating that the high-temperature and high-vacuum conditions did not induce measurable degradation. This structural stability enabled repeated reuse of the same foils for multiple irradiation and separation cycles, further improving process sustainability and cost-effectiveness.

V.5. Recovery Yield of ^{103}Pd

Following separation experiments employing niobium and ZnO-covered tungsten disc substrates, the deposited ^{103}Pd was recovered by acidic digestion and prepared for subsequent chemical processing. Recovery yields of approximately 77 ± 2% and 49 ± 2% were obtained for the niobium foil and ZnO-covered tungsten disc substrates, respectively. Experimental results showed that approximately 23% of the deposited ^{103}Pd remained unrecovered on the niobium foil, whereas nearly 51% diffused into the tungsten disc. The higher recovery yield observed for the niobium substrate can be attributed, at least in part, to its highly polished surface morphology. In contrast, the tungsten substrate exhibited a stronger tendency for palladium diffusion, even when neglecting the presence of the ZnO layer. These observations indicate that recovery efficiency is highly sensitive to substrate material properties, surface morphology, and operating temperature. At the same time, the experiments confirmed the anticipated role of ZnO as a diffusion barrier, although the applied thickness of 100 nm proved insufficient to fully suppress palladium penetration into the tungsten substrate.

In contrast, recovery of ^{103}Pd activity from the copper-coated alumina ceramic crucible substrate, following acidic extraction and subsequent purification, resulted in significantly higher recovery efficiencies ranging from 81% to 94%. This improvement in recovery yield demonstrates the effectiveness and feasibility of the upgrades implemented in the RSE configuration, particularly the selection of the alumina ceramic crucible substrate and the application of the copper coating to enhance deposition and recovery performance.

These results confirm the effectiveness of this novel wiping-based recovery approach, which complements the RSE dry-distillation process and provides a fully integrated separation–recovery workflow. This wiping-assisted acid extraction method has not been previously applied to dry-distilled palladium radionuclides, making it a novel and practical contribution to radiometal purification strategies. This combined strategy offers a promising alternative to conventional dissolution-based separation methods by enabling high recovery efficiencies with minimal substrate degradation and improved radionuclidic purity. The yield of separated ^{103}Pd obtained using the upgraded RSE configuration was substantial and sufficient to support subsequent preclinical investigations [105].

V.6. ICP-MS Quantification of Palladium Content in Rhodium Foils before and after RSE Processing

ICP-MS measurements demonstrated a clear and reproducible difference in palladium content between rhodium foils subjected to thermal treatment using the RSE and untreated reference foils. Specifically, the heated (treated) rhodium foils contained significantly lower palladium concentrations compared with the original untreated foils,

confirming the effective removal of residual (cold) palladium during the heating process (Figure 22).

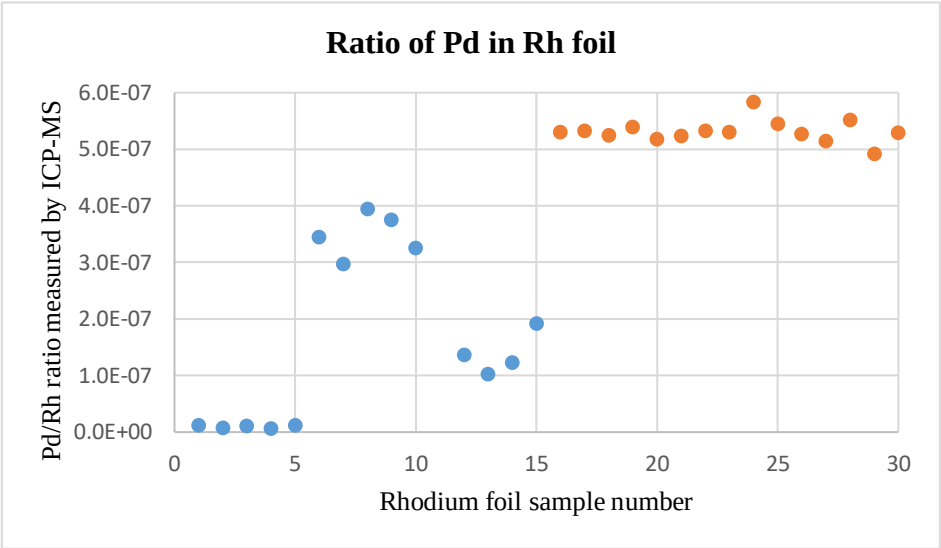

Figure 22. ICP-MS–determined Pd/Rh ratios in untreated and RSE-heated rhodium foils prior to irradiation. Orange symbols indicate untreated rhodium foils, while blue symbols indicate RSE-treated rhodium foils. Each data point represents an individual ICP-MS measurement. Three untreated and three RSE-treated rhodium foils were analyzed, with five replicate measurements performed for each foil.

A systematic variation in residual palladium content was observed among the three treated foils, which can be attributed to their relative positioning within the yttria-stabilized zirconia (YSZ) crucible. The foil positioned closest to the crucible wall exhibited the lowest palladium content, indicating the most efficient palladium evaporation. This effect is explained by enhanced thermal coupling at the crucible wall, where direct contact resulted in a higher local temperature compared with the foil positioned centrally within the crucible. The centrally located foil experienced reduced heat flux and, consequently, less efficient palladium volatilization. These observations highlight the sensitivity of the

separation process to temperature gradients and local heat transfer conditions within the crucible. These findings prompted a reconsideration of foil positioning and motivated further optimization of the heating configuration to achieve more homogeneous thermal conditions across all foils. Improved thermal uniformity is expected to enhance reproducibility and maximize palladium removal efficiency prior to irradiation.

Additionally, ICP-MS measurements were performed on the solutions obtained from recovery of volatilized cold palladium deposited on the copper-coated alumina ceramic crucible substrate. These solutions exhibited a clearly measurable palladium content, confirming that palladium removed from the heated rhodium foils was successfully collected and transferred into the liquid phase. The control solution prepared using the same recovery procedure applied to a clean alumina ceramic crucible substrate without copper coating showed palladium concentrations at or near the detection limit of the ICP-MS.

Importantly, the results demonstrate that preheating rhodium foils using the RSE prior to irradiation is a viable strategy for increasing the specific activity of the subsequently produced radioactive ^{103}Pd. High specific activity is a critical requirement for receptor-targeted radiopharmaceutical applications, as excess non-radioactive metal competes with the radiolabeled compound for receptor binding sites and reduces targeting efficiency at the cellular membrane level. This effect has been well documented for radiolabeled peptides, where increased specific activity directly enhances receptor-mediated uptake and targeting efficiency, while minimizing receptor saturation by non-radioactive species [65, 106].

The ICP-MS results further revealed that the concentrations of iridium (Ir) and ruthenium (Ru) remained approximately consistent between treated and untreated rhodium foils (Figures 23 and 24). This behavior is consistent with thermodynamic expectations, as the vapor pressures of iridium and ruthenium are lower than that of rhodium across the investigated temperature range. In contrast, palladium exhibits a vapor pressure at least two orders of magnitude higher than that of rhodium at the operating temperatures, enabling its selective volatilization. These observations provide independent experimental validation of the RSE concept, which relies on selective evaporation driven by differences in partial vapor pressures (Figure 25).

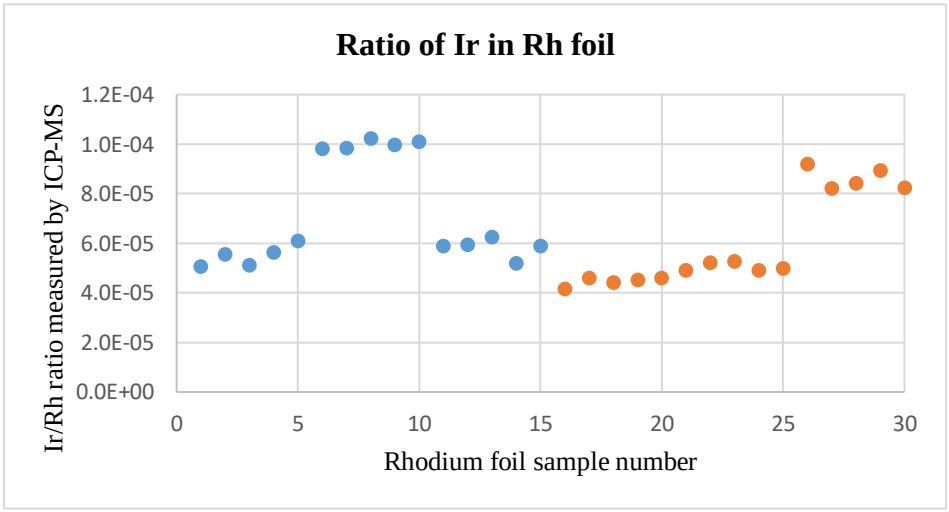

Figure 23. ICP-MS–determined Ir/Rh ratios in untreated and RSE-heated rhodium foils. Blue symbols indicate untreated rhodium foils, while orange symbols indicate RSE-treated rhodium foils. Each data point represents an individual ICP-MS measurement. Three untreated and three RSE-treated rhodium foils were analyzed, with five replicate measurements performed for each foil.

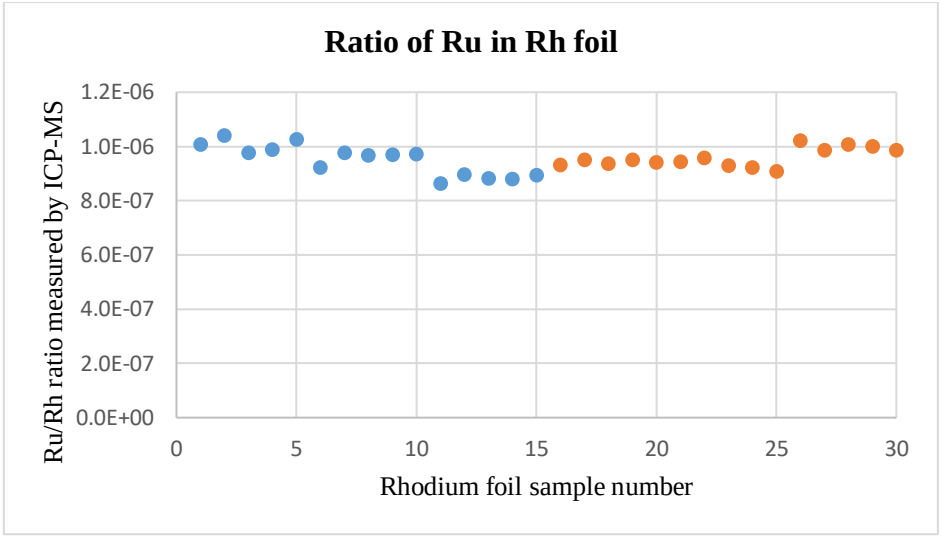

Figure 24. ICP-MS–determined Ru/Rh ratios in untreated and RSE-heated rhodium foils. Blue symbols indicate untreated rhodium foils, while orange symbols indicate RSE-treated rhodium foils. Each data point represents an individual ICP-MS measurement. Three untreated and three RSE-treated rhodium foils were analyzed, with five replicate measurements performed for each foil.

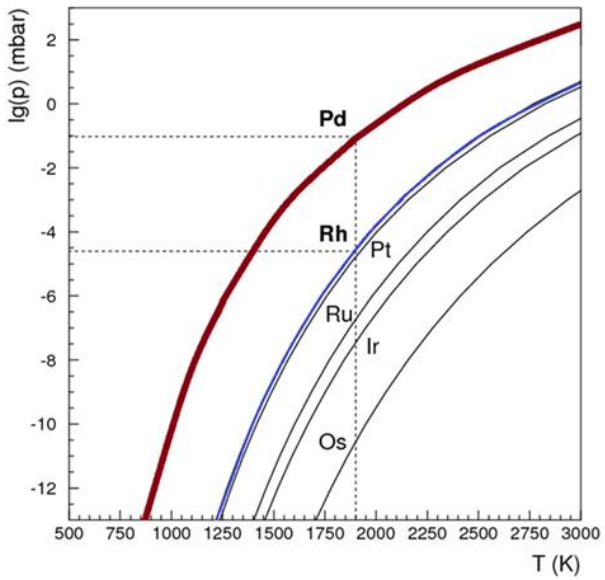

Figure 25. Vapor pressure comparison of palladium, rhodium, iridium, and ruthenium as a function of temperature.

In addition, ICP-MS analysis was performed on radioactive palladium separated using the earlier RSE configuration without preheating of the rhodium foils prior to irradiation. The rinsed ^{103}Pd activity collected in solution was analyzed to determine the total palladium mass, allowing calculation of the specific activity. The measured specific activity was 8.1 GBq·g^{-1}, confirming that the absence of pre-treatment results in a comparatively low specific activity. This finding further underscores the importance of pre-irradiation palladium removal to achieve radiochemically and biologically optimal ^{103}Pd preparations.

V.7. SEM Characterization of Surface Morphology of RSE-Processed and Unprocessed Rhodium Foils

Scanning electron microscopy (SEM) was employed to compare the surface morphology of the same six rhodium foils before and after thermal treatment using the RSE (Figure 26). SEM images revealed no discernible differences in surface topography, grain structure, or macroscopic features between the RSE-processed and unprocessed foils. No evidence of surface degradation, melting, cracking, or structural distortion was observed as a result of the thermal treatment. The preservation of surface morphology indicates that the RSE process does not adversely affect the mechanical or structural integrity of the rhodium foils. These observations demonstrate that the foils remain suitable for reuse in subsequent irradiation and separation cycles without compromising their physical integrity.

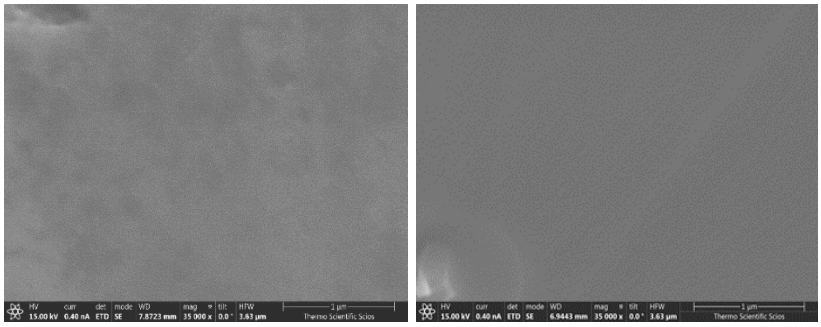

(**a**) (**b**)

Figure 26. SEM images of rhodium foils: (**a**) before; and (**b**) after thermal treatment using the RSE, demonstrating preserved surface morphology and structural integrity.

V.8. Evaluation of ^{103m}Rh Daughter Nuclide Release from ^{103}Pd-Complexes

Strata-X and Strata-C18 columns, both featuring reverse-phase polymeric sorbents, were employed to immobilize the [^{103}Pd]Pd–DOTA-TOC complex for recoil-effect studies of ^{103m}Rh daughter radionuclide release. For statistical robustness, four elutions of the [^{103}Pd]Pd–DOTA-TOC complex were performed for each column type (Strata-X and Strata-C18) at 24 h intervals over four consecutive days (n = 4). All eluates were analyzed immediately by gamma spectroscopy.

With a half-life of 56.1 min, the ^{103m}Rh daughter radionuclide reaches secular equilibrium with its ^{103}Pd parent after approximately five half-lives. Accordingly, maintaining a minimum interval of 5 h between successive elutions ensured equilibrium conditions during each measurement cycle [107]. In addition, this interval allowed for the complete decay of any residual ^{103m}Rh remaining on the column from the preceding elution step, thereby standardizing experimental conditions across all measurements. As illustrated in Figure 27, after five half-lives,

the regenerated ^{103m}Rh activity reaches approximately 97% of its theoretical equilibrium value, while residual activity from the previous cycle is reduced to about 3%.

The decay schemes of ^{103}Pd and ^{103m}Rh (Figure 28) show that 99.9% of ^{103}Pd decays to ^{103m}Rh at an excitation energy of 39.76 keV, and 100% of ^{103m}Rh subsequently decays to stable ^{103}Rh with emission of a 39.76 keV gamma photon (intensity: 0.068%). Thus, the difference in measured activity on the column before and after each washing step accurately represents the fraction (1/0.999) of ^{103m}Rh released into the eluate. A minor decrease in the intensity of the 357.5 keV gamma peak indicated a small leakage of ^{103}Pd from the chromatographic column; however, this contribution was neglected in the ^{103m}Rh activity calculations because measurements were conducted promptly, and any ^{103m}Rh generated from eluted ^{103}Pd during the measurement period contributed less than ~5% of the total activity measured.

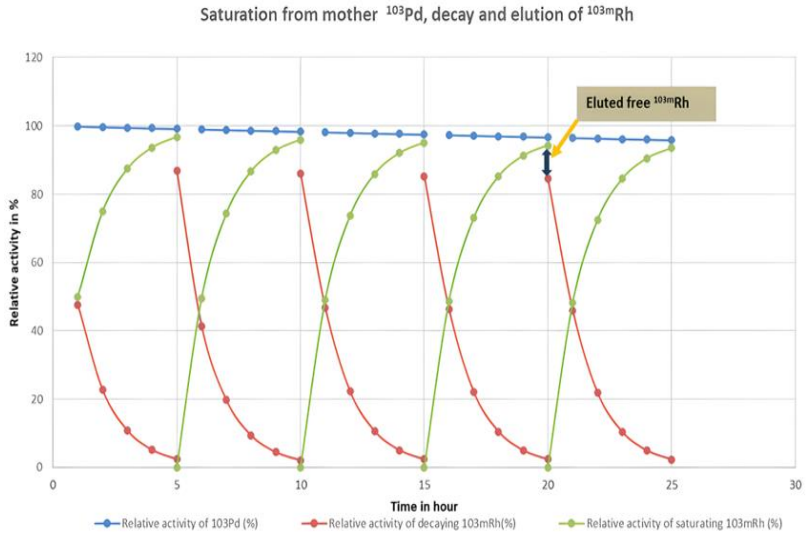

Figure 27. Relative activity ratio of ^{103}Pd and ^{103m}Rh retained on the Strata-X column over the course of the experiment.

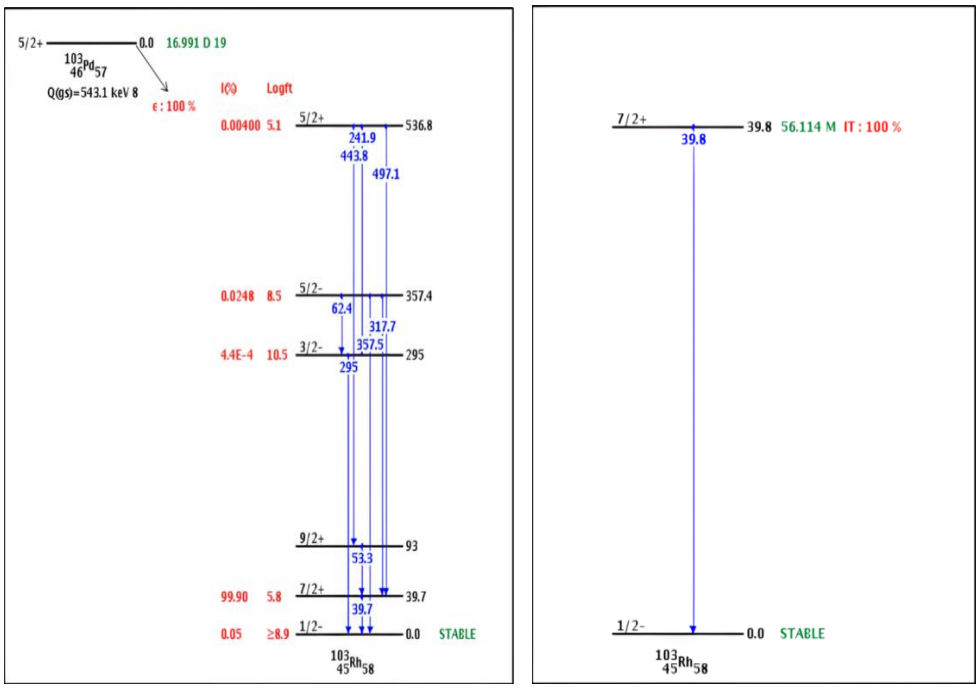

(**a**) (**b**)

Figure 28. Decay schemes of: (**a**) ^{103}Pd-radionuclide; (**b**) ^{103m}Rh-radionuclide, showing the transition of ^{103}Pd to ^{103m}Rh and subsequent decay to stable ^{103}Rh, along with associated gamma emissions [108].

The experimental data on the percentage of free ^{103m}Rh-radionuclide released from the complex and eluted from the different columns are summarized in Table 5. The variation in the measured values between columns is most likely due to the slight variation in geometry/positioning within the detector between the different individual columns which impacts the measurement of low energy gammas.

Table 5. Eluted ^{103m}Rh (%) from [^{103}Pd]Pd–DOTA-TOC (DC)–loaded Strata-X (n = 4) and Strata-C18 (n = 4) columns, indicating recoil-induced dissociation from chelator-bound complexes.

Elution Cycle	Eluted ^{103m}Rh (%) from the Strata-X column (n = 4)	Eluted ^{103m}Rh (%) from the Strata-C18 column (n = 4)
DC/1	5.0	12.3
DC/2	12.8	12.3
DC/3	10.6	11.0
DC/4	13.4	12.4
Average Eluted ^{103m}Rh (%)	10.5± 2.7	12.0 ± 0.5

The release of the daughter ^{103m}Rh radionuclide from the chelator-bound [^{103}Pd]Pd–DOTA-TOC complex was evaluated using both chromatographic column types. The average measured daughter release ratios were 10.5 ± 2.7% for Strata-X and 12.0 ± 0.5% for Strata-C18. Statistical analysis using Student's t-test revealed no significant difference between the two systems (P = 0.282). The release process in both column types is dominated by the highly localized and intense electronic excitation resulting from the Auger electron cascade, leading to comparable daughter nuclide release behavior. The theoretical Auger electron yield for ^{103}Pd decay is reported as ~186% [18]. Taken together, these results demonstrate that the ^{103m}Rh daughter release ratio is markedly lower than values previously predicted based on studies of other Auger electron–emitting radionuclides. For example, investigations of neodymium-140 (^{140}Nd) and dysprosium-166 (^{166}Dy) reported high correspondence between Auger

electron yields and daughter release, with approximately 95% release for ^{140}Nd (88% Auger yield) and 72% release for ^{166}Dy (75% Auger yield), reflecting a strong correlation between predicted electronic excitation and measured daughter dissociation [80, 109, 110]. In contrast, the behavior observed for the ^{103}Pd/^{103m}Rh system differs substantially from these trends. This further contrasts with the essentially quantitative release reported for francium-221 (^{221}Fr) in the Actinium-225 (^{225}Ac) decay system [111], as well as with the approximately 30% release of Bismuth-212 (^{212}Bi) from the Lead-212 (^{212}Pb) system [112]. Notably, both of these parent–daughter pairs have progressed to clinical evaluation, with ^{225}Ac currently advancing to Phase III clinical trials (ACTION trial). In this context, the observed release behavior of the ^{103}Pd/^{103m}Rh system compares favorably with clinically relevant radionuclide pairs and supports its potential for future clinical translation. These earlier correlations support the hypothesis that Auger electron cascades generate a dense local cloud of low-energy electrons, leading to electronic destabilization of the daughter ion–chelator complex rather than recoil-driven bond rupture. This interpretation is consistent with Szilárd's classical description of radioactive decay as a process that alters chemical states through electronic rearrangement rather than purely mechanical recoil effects [113]. One possible explanation for this unexpected deviation in the ^{103}Pd/^{103m}Rh system is that the true Auger electron yield may be closer to ~10% rather than the reported 186%, which is likely a calculated value. This discrepancy suggests inaccuracies in the currently reported nuclear decay data [114], warranting experimental reassessment and direct measurements of Auger electron yield; however, such work lies beyond the scope of this study.

Comparing the effective irradiation time of daughter radionuclides released from an Auger electron-therapeutic complex with their potential biological effects requires an understanding of ion transport at the molecular level, from the nuclide within a cell, across the cell membrane, and through active and passive transport (diffusion) in the interstitial and extracellular spaces of the body, as discussed in detail in reviews [6, 31]. Diffusion of small molecules in the cytoplasm is approximately four times slower than in water, but translational diffusion in cytoplasm still occurs in the millisecond range [115, 116]. Ion mobility through ion channels in the cell membrane is also rapid, occurring on the millisecond scale for cations, and this can similarly apply to arsenic-containing ions, which are known to initiate apoptosis [117, 118].

The chemical properties of these released radionuclide daughters also influence their radiation risk. The half-lives of these radionuclides typically range from hours to days [119], meaning that once released, they will decay within the body. As these radionuclides lack preferential organ-specific accumulation, they often bind to proteins in circulation and as a result, their radiation dose is primarily delivered to circulating blood, lymphatic fluids, and clearance organs such as the liver and kidneys. This highlights the need for careful evaluation of daughter radionuclide redistribution when designing Auger electron-based therapeutic agents. These risks are at this stage theoretical and warrant in vitro cell uptake or membrane transport studies to prove its effect though well-designed future radiobiology studies. The average measured daughter release investigated in this study was approximately 10% for the ^{103}Pd/^{103m}Rh *in vivo* generator system. Although this value is lower than initially anticipated and lower than that reported for other radionuclide systems, it is premature, in the

absence of dedicated in vitro radiobiological studies, to determine whether this level of release would result in clinically relevant off-target radiation.

V.9. Quality Control of [^{103}Pd]Pd–Radiolabeled NOTA and DOTA-TATE Complexes

V.9.1. Quality Control of [^{103}Pd]Pd–NOTA Complexes

Radiochemical purity (RCP) of the [^{103}Pd]Pd–NOTA complexes was assessed by instant thin-layer chromatography (iTLC) using methanol as the mobile phase and was determined to be approximately 95.7%. The signal corresponding to free palladium was negligible compared to the dominant [^{103}Pd]Pd–NOTA complex signal, confirming successful radiolabeling and suitability of the [^{103}Pd]Pd–NOTA complexes for injection into murine models.

V.9.2. Quality Control of [^{103}Pd]Pd–DOTA-TATE Complexes

Radiochemical purity (RCP) of the [^{103}Pd]Pd–DOTA-TATE complex was assessed using two complementary methods: solid-phase extraction (SPE)–based affinity chromatography and instant thin-layer chromatography (iTLC).

For SPE analysis, a Sep-Pak mini affinity chromatography column was preconditioned with 20 mL of methanol followed by 20 mL of Milli-Q water. A drop of the reaction mixture was then loaded onto the column and sequentially eluted with 8 mL of methanol (peptide-bound fraction) and 10 mL of Milli-Q water (free or ionic palladium fraction). The radioactivity of each fraction was measured, and the RCP was calculated as the ratio of activity in the methanol fraction to the total activity

recovered. Using this method, the RCP was determined to be approximately 92%.

In parallel, iTLC was performed using acetone as the mobile phase, in which the peptide-bound activity migrates with the solvent front. The chromatograms were analyzed using a Raytest Mini-GITA radio-TLC scanner (Figure 29). This method yielded an RCP of 96.38%, confirming efficient radiolabeling.

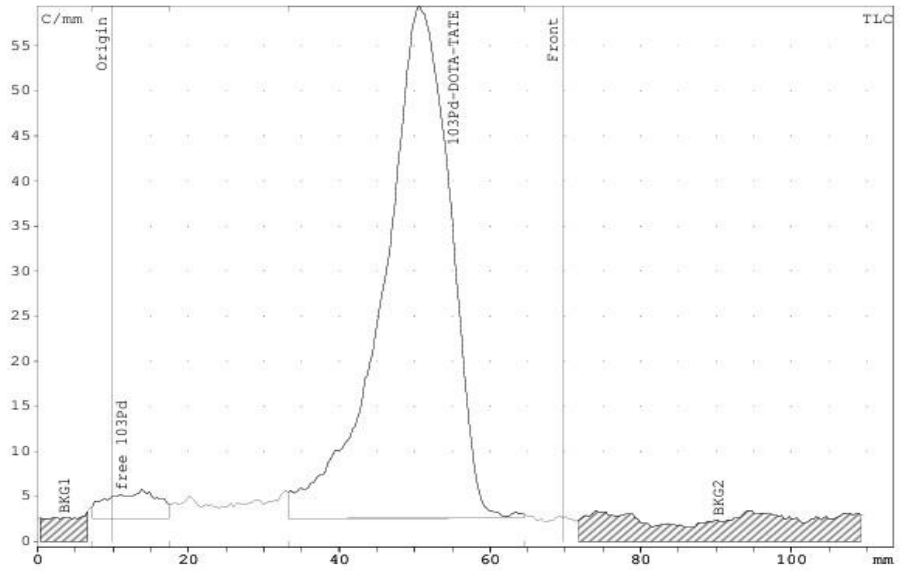

Figure 29. iTLC radiochromatographic analysis of [^{103}Pd]Pd–DOTA-TATE.

Following quality control, ~ 500 MBq of the [^{103}Pd]Pd–DOTA-TATE solution were diluted with physiological saline to a final volume of 2 mL and administered intravenously for subsequent in vivo applications.

V.10. SPECT/CT Imaging and Biodistribution of [^{103}Pd]Pd –NOTA in Murine Models

SPECT/CT imaging confirmed the expected ^{103}Pd photon emissions, and semi-quantitative tracer uptake was expressed as counts per milliliter (counts/mL). Serial acquisitions performed at 10 min, 1 day, and 3 days post-injection demonstrated stable radiolabeling and a consistent biodistribution profile, confirming the in vivo stability of the [^{103}Pd]Pd–NOTA-MAA. Figure 30 illustrates the biodistribution patterns and organ-specific tracer accumulation at these post-injection time points. This investigation demonstrates the feasibility of using NOTA-functionalized Macro-Aggregated Albumin Particles radiolabeled with ^{103}Pd for targeted delivery in particulate radioembolization of pulmonary metastases. In contrast to conventional microsphere therapies employing β-emitters such as yttrium-90 (^{90}Y) or lutetium-177 (^{177}Lu), which often result in broader radiation penetration and increased irradiation of healthy lung parenchyma [2, 120], ^{103}Pd provides a more confined dose distribution due to its low-energy emissions [121]. Furthermore, the short-range Auger electrons emitted by ^{103}Pd enable highly localized intratumoral energy deposition, minimizing radiation exposure to adjacent normal tissues. These characteristics highlight the theranostic potential of ^{103}Pd for targeted radiotherapy of lung lesions. For completeness, the corresponding imaging results obtained with the other investigated biomolecules (AMBA, cetuximab, and resin microspheres) are presented in the Appendix (Figures A1–A7).

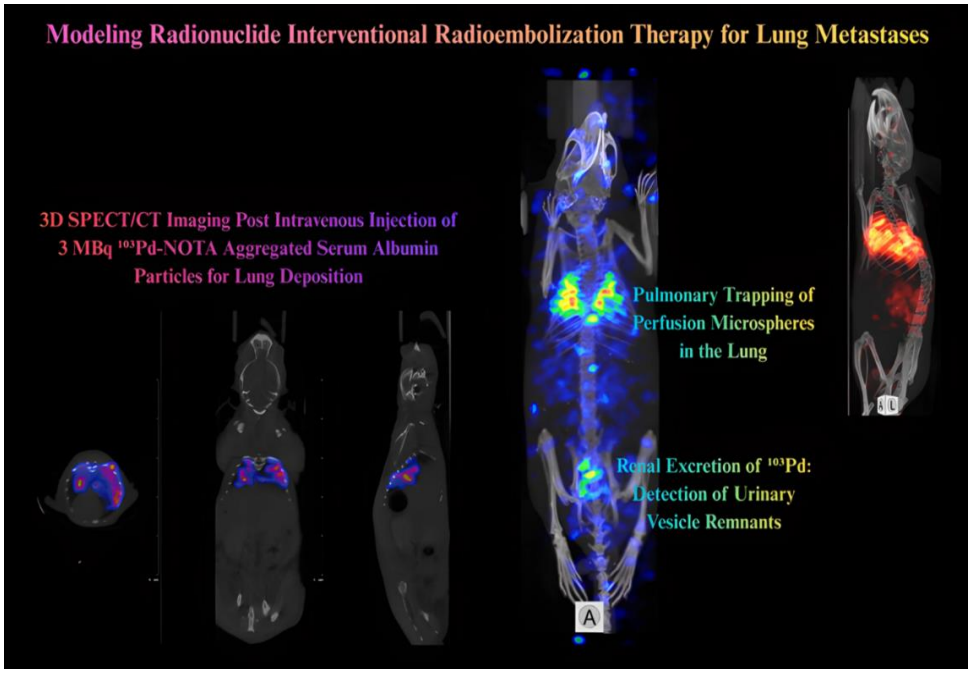

Figure 30. SPECT/CT images of [^{103}Pd]Pd–NOTA–MAA particles in a murine model, illustrating in vivo biodistribution in the lungs and excretion of decomposition products via the urinary system. The color scale represents SPECT activity, while grayscale corresponds to X-ray CT image reconstructions.

V.11. In Vivo SPECT/CT Evaluation of [^{103}Pd]Pd–DOTA-TATE in a Canine Model of Spontaneous Hepatic Malignancy

Serial SPECT/CT scans performed at 1 h, 24 h, 1 week, 2 weeks, and 4 weeks after administration demonstrated a slight reduction in tumor size in general (Figure 31). Follow-up clinical evaluation showed a marked improvement in the animal's previously hypoglycemia. The dog had initially exhibited low blood glucose levels, likely due to tumor-associated disturbances in glucose regulation. Hepatic malignancies can induce hypoglycemia through increased glucose consumption by rapidly proliferating tumor cells and impaired hepatic gluconeogenesis, leading to an imbalance between glucose demand and hepatic glucose production.

Consistent with these mechanisms, increase of blood glucose levels was observed during the follow-up period. Non-islet cell tumor hypoglycemia associated with hepatic tumors is often mediated by overproduction of incompletely processed insulin-like growth factor 2 (IGF-2), which exerts insulin-mimetic effects and contributes to persistent hypoglycemia [122, 123]. Continuous glucose monitoring (CGM) data showed an increase in average serum glucose levels from approximately 3.2 $mmol \cdot L^{-1}$ to 5.0 $mmol \cdot L^{-1}$ during the first two weeks of therapy, followed by stabilization at this level for a further two weeks. In contrast, insulin levels remained elevated after therapy. Clinically, the dog recovered strength and mobility, including the ability to walk using her hind limbs, representing a clear functional improvement compared to her debilitated state prior to treatment.

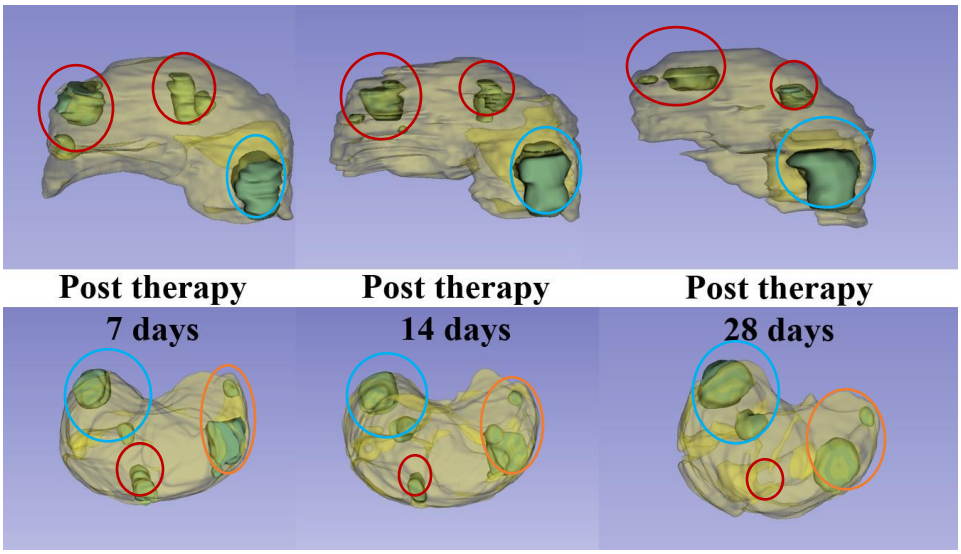

Figure 31. Threshold-based X-ray CT segmentation of metastatic liver tumor lesions in the dog at different time points post-therapy (7, 14, and 28 days). Red circles indicate tumor lesions that exhibited a reduction in size, blue circles indicate lesions that increased in size, and orange circles indicate lesions that remained stable without significant size change over the observation period.

X-ray CT–based segmentation and cross-sectional analysis demonstrated heterogeneous morphological responses of metastatic liver lesions following therapy. While some tumor foci exhibited a measurable reduction in volume, other lesions showed either limited growth or remained relatively stable in size, reflecting the intrinsically heterogeneous nature of metastatic tumor response. Nevertheless, when evaluated collectively, the overall tumor burden indicated a slight but consistent reduction. This trend is particularly evident in the cross-sectional CT images (Figure 32), where two clearly distinguishable tumor lesions are visible one day post-administration, whereas only a single lesion remains detectable after one week. The disappearance of one lesion from the later image strongly suggests a localized therapeutic response, supporting the conclusion that the applied treatment induced a net antitumor effect despite inter-lesional variability.

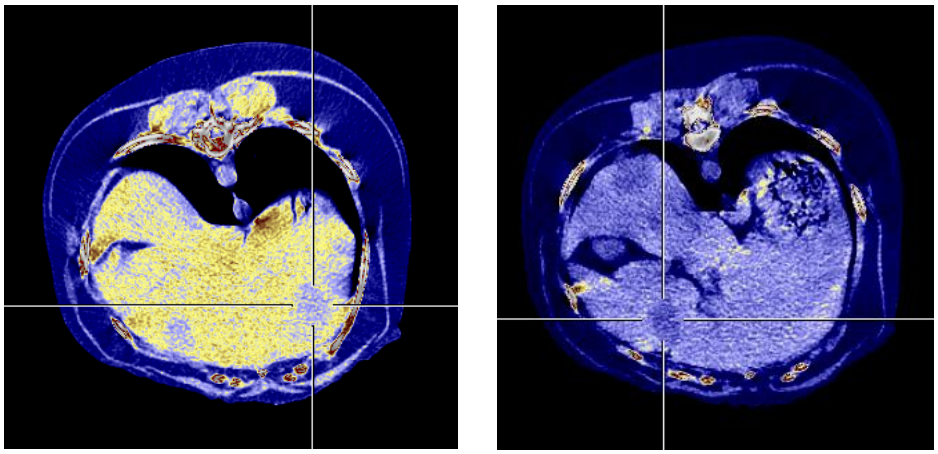

(**a**) (**b**)

Figure 32. X-ray CT cross-sectional images of metastatic liver tumor lesions in the canine model acquired (a) 1 day and (b) 1 week after therapy, illustrating early post-treatment morphological changes.

VI. Summary

This research establishes a complete and integrated workflow for the production, separation, purification, chelation, daughter radionuclide release evaluation from the ^{103}Pd/^{103m}Rh in vivo generator system, and preclinical evaluation of ^{103}Pd, demonstrating its feasibility as a theranostic Auger electron–emitting radionuclide. A central innovation of this work is the development and validation of a diffusion-driven dry-distillation approach for radionuclide separation, which exploits intrinsic differences in vapor pressure between palladium and rhodium following cyclotron irradiation of ^{103}Rh. This approach represents a credible and efficient alternative to conventional wet-chemistry–based separation methods, which are limited by rhodium's chemical inertness, prolonged processing times, lower overall yields, and the generation of large volumes of radioactive waste.

Cyclotron irradiation of ^{103}Rh for the production of ^{103}Pd was systematically optimized, and a proton energy of 11 MeV was identified as optimal. This energy lies near the maximum of the ^{103}Rh(p,n)^{103}Pd excitation function and provides a favorable balance between production yield and radionuclidic purity. In parallel, palladium–rhodium alloy samples were synthesized and investigated to characterize palladium diffusivity within a rhodium matrix and to estimate intrinsic diffusion coefficients relevant to the separation process. The chemical purity of the deposited palladium layers was assessed using surface analytical techniques, supported by systematic measurements on non-radioactive powder samples, which indicated no significant rhodium contamination in the deposited material.

Initial separation experiments identified challenges related to the efficient collection of volatilized ^{103}Pd and the prevention of alloy formation between palladium and the deposition substrate. These limitations motivated systematic optimization and subsequent upgrading of the radionuclide separation equipment (RSE). The improved RSE configuration, incorporating optimized thermal management, refined substrate selection, and enhanced recovery methodology, achieved high separation efficiencies of 64–86% and recovery yields of 81–94%. This represents a substantial improvement over both earlier RSE designs and traditional dissolution-based approaches. The dry-distillation method proved to be rapid, scalable, and well suited for repeated irradiations and high-throughput radionuclide production while significantly reducing radioactive waste generation. Additionally, both the deposition substrates and rhodium foils retained their structural integrity following RSE processing, enabling their reuse in subsequent irradiation and separation cycles.

ICP-MS measurements demonstrated a clear and reproducible reduction in palladium content in rhodium foils subjected to thermal pre-treatment using the RSE compared with untreated reference foils. These results confirm that preheating rhodium foils prior to irradiation effectively removes residual (cold) palladium and thereby enables a significant increase in the specific activity of the subsequently produced ^{103}Pd.

The release dynamics of the daughter radionuclide ^{103m}Rh from the ^{103}Pd/^{103m}Rh in vivo generator system were investigated via the Szilárd–Chalmers effect. Measurable daughter release from chelator-bound [^{103}Pd]Pd–DOTA-TOC complexes was observed, with mean release

fractions of 10.5 ± 2.7% and 12.0 ± 0.5% for Strata-X and Strata-C18 systems, respectively. These values are markedly lower than those reported for other Auger electron-emitting radionuclide systems, such as $^{225}Ac/^{221}Fr$ and $^{212}Pb/^{212}Bi$, which have already progressed to clinical evaluation. Importantly, the relatively low daughter release observed for the $^{103}Pd/^{103m}Rh$ system represents a favorable characteristic for potential clinical translation, as it suggests a reduced risk of off-target radiation from liberated daughter nuclides.

The discrepancy between the experimentally observed release fraction (~10%) and the theoretically predicted Auger electron yield (~186%) indicates that daughter release is not governed by nuclear recoil, but rather by localized electronic destabilization induced by Auger electron cascades. This interpretation is consistent with the classical Szilárd–Chalmers concept of decay-induced alterations of chemical states and highlights the need for improved nuclear and atomic-level characterization of Auger electron processes, as well as potential refinement of existing decay data.

Radiolabeling studies demonstrated that ^{103}Pd can be efficiently chelated using NOTA and DOTA-TATE, maintaining high radiochemical purity and in vivo stability. SPECT/CT imaging confirmed favorable biodistribution profiles and enabled longitudinal monitoring. Compared with established β-emitting radionuclides such as ^{90}Y and ^{177}Lu, ^{103}Pd offers distinct advantages for localized therapy owing to its low-energy photon emissions and subcellular-range Auger electrons, enabling highly confined intratumoral energy deposition while minimizing irradiation of surrounding healthy tissue. Preliminary translational evaluation in a spontaneous canine liver cancer model further supported the therapeutic

potential of ^{103}Pd. Although exploratory, the observed tumor size reduction and marked improvement in clinical condition suggest a biologically meaningful response and provide a strong rationale for continued investigation.

Collectively, this work integrates advances in nuclear physics, radiochemistry, materials science, and preclinical imaging, positioning ^{103}Pd as a compelling candidate for targeted Auger electron therapy. Future studies should focus on refined dosimetric modeling, comprehensive radiobiological evaluation, and direct comparison with other Auger electron-emitting systems to fully elucidate its therapeutic window and clinical translation potential. The principal scientific novelties and milestones achieved in this work are summarized below:

- Development of a diffusion-driven dry-distillation method for ^{103}Pd separation from irradiated ^{103}Rh targets.
- Engineering optimization of the radionuclide separation equipment (RSE) achieving separation efficiencies of 64–86% and recovery yields of 81–94%.
- Identification of 11 MeV as the optimal proton energy for the ^{103}Rh(p,n) ^{103}Pd reaction.
- Experimental investigation of palladium diffusion behavior within a rhodium matrix supporting the separation mechanism.
- Increase of ^{103}Pd specific activity through thermal pre-treatment of rhodium foils confirmed by ICP-MS.
- Systematic evaluation of daughter radionuclide release in the ^{103}Pd/^{103m}Rh in vivo generator system.
- Successful radiolabeling of ^{103}Pd with NOTA and DOTA-TATE with high radiochemical purity and stability.

- Preclinical SPECT/CT imaging evaluation of ^{103}Pd-labeled constructs in murine models.
- Preliminary translational evaluation in a spontaneous canine liver cancer model demonstrating tumor uptake and early therapeutic response.

VII. Résumé

Cette recherche établit un flux de travail complet et intégré pour la production, la séparation, la purification, la chélation, l'évaluation de la libération du radionucléide fils à partir du système générateur in vivo ^{103}Pd/^{103m}Rh, ainsi que l'évaluation préclinique du ^{103}Pd, démontrant ainsi sa faisabilité en tant que radionucléide théranostique émetteur d'électrons Auger. Une innovation majeure de ce travail réside dans le développement et la validation d'une approche de séparation par distillation sèche gouvernée par diffusion, exploitant les différences intrinsèques de pression de vapeur entre le palladium et le rhodium après irradiation cyclotron du ^{103}Rh. Cette méthode constitue une alternative crédible et efficace aux procédés conventionnels de séparation par chimie humide, lesquels sont limités par l'inertie chimique du rhodium, des temps de traitement prolongés, des rendements globaux plus faibles et la production de volumes importants de déchets radioactifs.

L'irradiation cyclotron du ^{103}Rh pour la production du ^{103}Pd a été systématiquement optimisée, et une énergie protonique de 11 MeV a été identifiée comme optimale. Cette énergie se situe à proximité du maximum de la fonction d'excitation de la réaction ^{103}Rh(p,n) ^{103}Pd et offre un compromis favorable entre rendement de production et pureté radionuclidique. En parallèle, des alliages palladium–rhodium ont été synthétisés et étudiés afin de caractériser la diffusivité du palladium dans une matrice de rhodium et d'estimer les coefficients de diffusion intrinsèques pertinents pour le processus de séparation. La pureté chimique des couches de palladium déposées a été évaluée par des techniques d'analyse de surface, appuyées par des mesures systématiques sur des échantillons de poudre non radioactive, lesquelles ont confirmé l'absence de contamination significative en rhodium.

Les premières expériences de séparation ont mis en évidence des difficultés liées à la collecte efficace du ^{103}Pd volatilisé et à la prévention de la formation d'alliages entre le palladium et le substrat de dépôt. Ces limitations ont conduit à une optimisation systématique et à l'amélioration de l'équipement de séparation radionuclidique (RSE). La configuration améliorée du RSE, intégrant une gestion thermique optimisée, une sélection affinée des substrats et une méthodologie de récupération renforcée, a permis d'atteindre des efficacités de séparation de 64 à 86 % et des rendements de récupération de 81 à 94 %. Ces performances représentent une amélioration substantielle par rapport aux conceptions antérieures du RSE ainsi qu'aux approches classiques basées sur la dissolution. La méthode de distillation sèche s'est révélée rapide, évolutive et adaptée aux irradiations répétées ainsi qu'à une production radionuclidique à haut débit, tout en réduisant significativement la génération de déchets radioactifs. De plus, les substrats de dépôt et les feuilles de rhodium ont conservé leur intégrité structurale après le traitement RSE, permettant leur réutilisation lors de cycles ultérieurs d'irradiation et de séparation.

Les mesures ICP-MS ont démontré une diminution claire et reproductible de la teneur en palladium dans les feuilles de rhodium soumises au prétraitement thermique par le RSE par rapport aux feuilles de référence non traitées. Ces résultats confirment que le préchauffage des feuilles de rhodium avant irradiation permet d'éliminer efficacement le palladium résiduel (froid) et d'augmenter significativement l'activité spécifique du ^{103}Pd produit ultérieurement.

La dynamique de libération du radionucléide fils ^{103m}Rh à partir du système générateur in vivo ^{103}Pd/^{103m}Rh a été étudiée via l'effet Szilárd–Chalmers. Une libération mesurable du radionucléide fils à partir des complexes [^{103}Pd]Pd–DOTA-TOC chélatés a été observée, avec des fractions moyennes de libération de 10,5 ± 2,7 % et 12,0 ± 0,5 % pour les systèmes Strata-X et Strata-C18, respectivement. Ces valeurs sont nettement inférieures à celles rapportées pour d'autres systèmes émetteurs d'électrons Auger, tels que ^{225}Ac/^{221}Fr et ^{212}Pb/^{212}Bi, déjà évalués cliniquement. La faible libération observée pour le système ^{103}Pd/^{103m}Rh constitue ainsi une caractéristique favorable pour une translation clinique potentielle, car elle suggère un risque réduit d'irradiation hors cible dû aux radionucléides fils libérés.

La divergence entre la fraction de libération expérimentale (~10 %) et le rendement théorique en électrons Auger (~186 %) indique que la libération du radionucléide fils n'est pas gouvernée par le recul nucléaire, mais plutôt par une déstabilisation électronique locale induite par les cascades Auger. Cette interprétation est cohérente avec le concept classique de Szilárd–Chalmers relatif aux modifications chimiques induites par la désintégration et souligne la nécessité d'une caractérisation plus approfondie des processus Auger aux niveaux nucléaire et atomique, ainsi qu'une éventuelle révision des données de désintégration existantes.

Les études de radiomarquage ont démontré que le ^{103}Pd peut être efficacement chélaté par NOTA et DOTA-TATE, tout en maintenant une pureté radiochimique élevée et une stabilité in vivo satisfaisante. L'imagerie SPECT/CT a confirmé des profils de biodistribution favorables et permis un suivi longitudinal. Comparé aux radionucléides β^- émetteurs établis tels que ^{90}Y et ^{177}Lu, le ^{103}Pd présente des avantages distincts pour les thérapies localisées grâce à ses émissions photonique de faible énergie et à ses électrons

Auger de portée subcellulaire, permettant un dépôt d'énergie intratumoral hautement confiné tout en minimisant l'irradiation des tissus sains environnants. L'évaluation translationnelle préliminaire réalisée dans un modèle canin spontané de cancer hépatique a renforcé le potentiel thérapeutique du ^{103}Pd. Bien que de nature exploratoire, la réduction observée de la taille tumorale et l'amélioration marquée de l'état clinique suggèrent une réponse biologique significative et justifient pleinement la poursuite des investigations.

Dans son ensemble, ce travail intègre des avancées en physique nucléaire, radiochimie, science des matériaux et imagerie préclinique, positionnant le ^{103}Pd comme un candidat prometteur pour la thérapie ciblée par électrons Auger. Les études futures devront se concentrer sur une modélisation dosimétrique approfondie, une évaluation radiobiologique complète et une comparaison directe avec d'autres systèmes émetteurs d'électrons Auger afin de définir pleinement sa fenêtre thérapeutique et son potentiel de translation clinique. Les principales innovations scientifiques et avancées majeures de ce travail sont résumées ci-dessous:

- Développement d'une méthode de séparation par distillation sèche contrôlée par diffusion pour l'extraction du ^{103}Pd à partir de cibles irradiées de ^{103}Rh.
- Optimisation technique de l'équipement de séparation des radionucléides (RSE), permettant d'atteindre des efficacités de séparation de 64 à 86 % et des rendements de récupération de 81 à 94 %.
- Identification de 11 MeV comme énergie protonique optimale pour la réaction nucléaire ^{103}Rh(p,n) ^{103}Pd.

- Étude expérimentale du comportement de diffusion du palladium dans une matrice de rhodium, permettant de mieux comprendre le mécanisme de séparation.
- Augmentation de l'activité spécifique du ^{103}Pd grâce à un prétraitement thermique des feuilles de rhodium, confirmée par des analyses ICP-MS.
- Évaluation systématique de la libération du radionucléide fils dans le système générateur in vivo ^{103}Pd/^{103m}Rh.
- Radiomarquage efficace du ^{103}Pd avec les chélateurs NOTA et DOTA-TATE, présentant une pureté radiochimique et une stabilité élevées.
- Évaluation préclinique par imagerie SPECT/CT de composés marqués au ^{103}Pd dans des modèles murins.
- Évaluation translationnelle préliminaire dans un modèle canin de cancer hépatique spontané, démontrant une accumulation tumorale et une réponse thérapeutique précoce.

VIII. References

1. Gudkov, S.V., et al., *Targeted radionuclide therapy of human tumors.* International journal of molecular sciences, 2015. **17**(1): p. 33.

2. Wang, J.S., et al., *Diffuse pneumonitis after Lutetium-177-PSMA-617 treatment in a patient with metastatic castration-resistant prostate cancer.* BMJ Case Reports CP, 2024. **17**(2): p. e257772.

3. Kim, Y.-S. and M.W. Brechbiel, *An overview of targeted alpha therapy.* Tumor biology, 2012. **33**(3): p. 573-590.

4. Tranel, J., et al., *Effect of microdistribution of alpha and beta-emitters in targeted radionuclide therapies on delivered absorbed dose in a GATE model of bone marrow.* Physics in Medicine & Biology, 2021. **66**(3): p. 035016.

5. O'donoghue, J. and T. Wheldon, *Targeted radiotherapy using Auger electron emitters.* Physics in Medicine & Biology, 1996. **41**(10): p. 1973.

6. Ku, A., et al., *Auger electrons for cancer therapy–a review.* EJNMMI radiopharmacy and chemistry, 2019. **4**(1): p. 27.

7. Falzone, N., et al., *Monte Carlo evaluation of Auger electron–emitting theranostic radionuclides.* Journal of Nuclear Medicine, 2015. **56**(9): p. 1441-1446.

8. Behr, T.M., et al., *Therapeutic advantages of Auger electron-over β-emitting radiometals or radioiodine when conjugated to internalizing*

antibodies. European journal of nuclear medicine, 2000. **27**(7): p. 753-765.

9. Reissig, F., et al., *Direct and Auger electron-induced, single-and double-strand breaks on plasmid DNA caused by 99mTc-labeled pyrene derivatives and the effect of bonding distance.* PLoS One, 2016. **11**(9): p. e0161973.

10. Pirovano, G., T.C. Wilson, and T. Reiner, *Auger: The future of precision medicine.* Nuclear medicine and biology, 2021. **96**: p. 50-53.

11. Stap, J., et al., *Induction of linear tracks of DNA double-strand breaks by α-particle irradiation of cells.* Nature methods, 2008. **5**(3): p. 261-266.

12. Moradi, M.S. and B.S. Bidabadi, *Assessment of single-and double-strand breaks in DNA induced by auger electrons of radioisotopes used in diagnostic and therapeutic applications.* Journal of Medical Physics, 2020. **45**(4): p. 240-248.

13. Caldecott, K.W., *DNA single-strand break repair and human genetic disease.* Trends in cell biology, 2022. **32**(9): p. 733-745.

14. Wang, W., et al., *Modelling of cellular survival following radiation-induced DNA double-strand breaks.* Scientific reports, 2018. **8**(1): p. 16202.

15. Parsi, M., et al., *PSMA: a game changer in the diagnosis and treatment of advanced prostate cancer.* Medical Oncology, 2021. **38**(8): p. 89.

16. Ahmadi, P., M.S.Z. Ghandi, and A. Shokri, *Investigation of Auger Electron Emitting Radionuclides Effects in Therapy Using the Geant4-DNA Toolkit: A Simulation Study.* Frontiers in Biomedical Technologies, 2021. **8**(2): p. 79-86.

17. Ferro, A., et al., *Reductions in prostatic doses are associated with less acute morbidity in patients undergoing Pd-103 brachytherapy: Substantiation of the rationale for focal therapy.* Brachytherapy, 2018. **17**(2): p. 313-318.

18. ENSDF, I., *Live Chart of Nuclides nuclear structure and decay data*. 2019.

19. Firestone, R.B., *The table of isotopes-and beyond.* Transactions of the American Nuclear Society, 1996. **75**(CONF-961103-).

20. Khan, F.M., *The Physics of Radiation Therapy, Lippincott, Williams & Wilkins*. 2010, Baltimore, MD.

21. Pomplun, E. and M. Terrissol, *Low-energy electrons inside active DNA models: a tool to elucidate the radiation action mechanisms.* Radiation and environmental biophysics, 1994. **33**(4): p. 279-292.

22. Gümüş, H. and A. Bentabet, *CSDA range, stopping power and mean penetration depth energy relationships in some hydrocarbons and biologic materials for 10 eV to 100 MeV with the modified Rohrlich–Carlson model.* Applied Physics A, 2017. **123**(5): p. 334.

23. Sudár, S., F. Cserpák, and S. Qaim, *Measurements and nuclear model calculations on proton-induced reactions on 103Rh up to 40 MeV: evaluation of the excitation function of the 103Rh (p, n) 103Pd reaction*

relevant to the production of the therapeutic radionuclide 103Pd. Applied radiation and isotopes, 2002. **56**(6): p. 821-831.

24. AC07607271, A., *Cyclotron produced radionuclides-physical characteristics and production methods. Internat.* Atomic Energy Agency, 2009.

25. Tavares, A.A.S. and J.M.R. Tavares, *99mTc Auger electrons for targeted tumour therapy: A review.* International journal of radiation biology, 2010. **86**(4): p. 261-270.

26. Unak, P., *Targeted tumor radiotherapy.* Brazilian Archives of Biology and Technology, 2002. **45**: p. 97-110.

27. Nikoloski, A.N., K.-L. Ang, and D. Li, *Recovery of platinum, palladium and rhodium from acidic chloride leach solution using ion exchange resins.* Hydrometallurgy, 2015. **152**: p. 20-32.

28. Laouameria, A.N., et al., *Innovative Approach to Producing Palladium-103 for Auger-Emitting Radionuclide Therapy: A Proof-of-Concept Study.* Pharmaceuticals, 2024. **17**(2): p. 253.

29. Alekseev, I., *Diffusion-thermal methods for radionuclides isolation from solid-state reactor and cyclotron targets: possible prospects.* 2003.

30. van Rooyen, J., Z. Szucs, and J.R. Zeevaart, *A possible in vivo generator 103Pd/103mRh—Recoil considerations.* Applied Radiation and Isotopes, 2008. **66**(10): p. 1346-1349.

31. Edem, P.E., et al., *In vivo radionuclide generators for diagnostics and therapy.* Bioinorganic Chemistry and Applications, 2016. **2016**(1): p. 6148357.

32. Hope, T.A., et al., *Appropriate use criteria for somatostatin receptor PET imaging in neuroendocrine tumors.* Journal of Nuclear Medicine, 2018. **59**(1): p. 66-74.

33. Hermanson, G.T., *Bioconjugate techniques*. 2013: Academic press.

34. Chandekar, K.R. and C. Bal. *Advances With 225Ac-DOTATATE Targeted Alpha Therapy in Somatostatin Receptor Positive Neuroendocrine Tumors*. in *Seminars in nuclear medicine*. 2025. Elsevier.

35. Zheng, Y., et al., *Simultaneous imaging of Ga-DOTA-TATE and Lu-DOTA-TATE in murine models of neuroblastoma.* IEEE transactions on radiation and plasma medical sciences, 2022. **7**(1): p. 75-82.

36. Dash, A., F. F. Knapp, and M. Ra Pillai, *Targeted radionuclide therapy-an overview.* Current radiopharmaceuticals, 2013. **6**(3): p. 152-180.

37. O'donoghue, J., M. Bardies, and T. Wheldon, *Relationships between tumor size and curability for uniformly targeted therapy with beta-emitting radionuclides.* Journal of Nuclear Medicine, 1995. **36**(10): p. 1902-1909.

38. Kwekkeboom, D.J., et al., *Treatment with the radiolabeled somatostatin analog [177Lu-DOTA0, Tyr3] octreotate: toxicity,*

efficacy, and survival. Journal of clinical oncology, 2008. **26**(13): p. 2124-2130.

39. de Keizer, B., et al., *Hormonal crises following receptor radionuclide therapy with the radiolabeled somatostatin analogue [177Lu-DOTA0, Tyr3] octreotate.* European journal of nuclear medicine and molecular imaging, 2008. **35**(4): p. 749-755.

40. Strosberg, J., et al., *Phase 3 trial of 177Lu-Dotatate for midgut neuroendocrine tumors.* New England Journal of Medicine, 2017. **376**(2): p. 125-135.

41. Bodei, L., et al., *Long-term evaluation of renal toxicity after peptide receptor radionuclide therapy with 90Y-DOTATOC and 177Lu-DOTATATE: the role of associated risk factors.* European journal of nuclear medicine and molecular imaging, 2008. **35**(10): p. 1847-1856.

42. Cremonesi, M., et al., *Dosimetry for treatment with radiolabelled somatostatin analogues. A review.* The Quarterly Journal of Nuclear Medicine and Molecular Imaging, 2010. **54**(1): p. 37.

43. Kratochwil, C., et al., *225Ac-PSMA-617 for PSMA-targeted α-radiation therapy of metastatic castration-resistant prostate cancer.* Journal of Nuclear Medicine, 2016. **57**(12): p. 1941-1944.

44. Parker, C., et al., *Alpha emitter radium-223 and survival in metastatic prostate cancer.* New England Journal of Medicine, 2013. **369**(3): p. 213-223.

45. McDevitt, M.R., et al., *Radioimmunotherapy with alpha-emitting nuclides.* European journal of nuclear medicine, 1998. **25**(9): p. 1341-1351.

46. Kozempel, J., O. Mokhodoeva, and M. Vlk, *Progress in targeted alpha-particle therapy. What we learned about recoils release from in vivo generators.* Molecules, 2018. **23**(3): p. 581.

47. Radchenko, V., J.W. Engle, and H. Thisgaard, *Status and future perspectives of Meitner-Auger and low energy electron-emitting radionuclides for targeted radionuclide therapy*. 2021. p. 106.

48. Vaidyanathan, G., et al., *Synthesis and preliminary evaluation of 211At-labeled inhibitors of prostate-specific membrane antigen for targeted alpha particle therapy of prostate cancer*. Nuclear medicine and biology, 2021. **94**: p. 67-80.

49. Repetto, M., J. Semprine, and A. Boveris, *Lipid peroxidation: Chemical mechanism, biological implications and analytical.* Lipid peroxidation, 2012: p. 1.

50. Dixon, S.J., et al., *Ferroptosis: an iron-dependent form of nonapoptotic cell death.* cell, 2012. **149**(5): p. 1060-1072.

51. Tekin, V., et al., *A novel anti-angiogenic radio/photo sensitizer for prostate cancer imaging and therapy: 89Zr-Pt@ TiO2-SPHINX, synthesis and in vitro evaluation.* Nuclear Medicine and Biology, 2021. **94**: p. 20-31.

52. Filosofov, D., E. Kurakina, and V. Radchenko, *Potent candidates for Targeted Auger Therapy: Production and radiochemical considerations.* Nuclear Medicine and Biology, 2021. **94**: p. 1-19.

53. Wang, J., et al., *Direct labeling of a somatostatin receptor antagonist via peptide cyclization with Re, 99mTc and 186Re metal centers: Radiochemistry and in vitro evaluation.* Nuclear Medicine and Biology, 2021. **94**: p. 46-52.

54. Driver, C.H., et al., *Towards the development of a targeted albumin-binding radioligand for theranostic applications: synthesis, radiolabelling and preliminary in vivo studies.* 2020.

55. Silverman, I., et al., *Production of Palladium-103 (103Pd) from a thin rhodium foil target–Improved cooling concept.* Nuclear Instruments and Methods in Physics Research Section B: Beam Interactions with Materials and Atoms, 2007. **261**(1-2): p. 747-750.

56. Eckerman, K. and A. Endo, *ICRP Publication 107. Nuclear decay data for dosimetric calculations.* Annals of the ICRP, 2008. **38**(3): p. 7-96.

57. Nag, S., et al., *American Brachytherapy Society (ABS) recommendations for transperineal permanent brachytherapy of prostate cancer.* International Journal of Radiation Oncology* Biology* Physics, 1999. **44**(4): p. 789-799.

58. Rivard, M.J., et al., *Update of AAPM Task Group No. 43 Report: A revised AAPM protocol for brachytherapy dose calculations.* Medical physics, 2004. **31**(3): p. 633-674.

59. Bolcaen, J., et al., *Marshalling the potential of Auger electron radiopharmaceutical therapy*. Journal of Nuclear Medicine, 2023. **64**(9): p. 1344-1351.

60. Humm, J.L., R.W. Howell, and D.V. Rao, *Dosimetry of Auger-electron-emitting radionuclides: report no. 3 of AAPM Nuclear Medicine Task Group No. 6.* Medical physics, 1994. **21**(12): p. 1901-1915.

61. Qaim, S., *Cyclotron production of medical radionuclides*, in *Handbook of nuclear chemistry*. 2011, Springer. p. 1903-1933.

62. IAEA. and IAEA., *Cyclotron Produced Radionuclides*. 2009: International Atomic Energy Agency.

63. Mausner, L., et al., *Production of 103Pd by proton irradiation of silver.* Journal of Labelled Compounds and Radiopharmaceuticals, 2001. **44**(S1): p. S775-S777.

64. Zagryadsky, V., et al., *MEASUREMENT OF THE RATES OF THE 102Pd.* Âdernaâ fizika, 2024. **87**(5): p. 365-368.

65. Breeman, W.A., et al., *Optimising conditions for radiolabelling of DOTA-peptides with 90Y, 111In and 177Lu at high specific activities.* European journal of nuclear medicine and molecular imaging, 2003. **30**(6): p. 917-920.

66. Saidi, P. and M. Sadeghi, *Production of the 103 Pd via Cyclotron and Preparation of the Brachytherapy Seed*, in *Recent Techniques and Applications in Ionizing Radiation Research*. 2020, IntechOpen.

67. Synowiecki, M.A., L.R. Perk, and J.F.W. Nijsen, *Production of novel diagnostic radionuclides in small medical cyclotrons.* EJNMMI radiopharmacy and chemistry, 2018. **3**(1): p. 3.

68. Hermanne, A., et al., *Study on production of 103Pd and characterisation of possible contaminants in the proton irradiation of 103Rh up to 28 MeV.* Nuclear Instruments and Methods in Physics Research Section B: Beam Interactions with Materials and Atoms, 2000. **170**(3-4): p. 281-292.

69. Van Puymbroeck, J. and R. Gijbels, *The average cross section of the 102Pd (n, p) 102,102 mRh and 103Rh (n, 2n) 102, 102m Rh reactions in a fission neutron spectrum.* Journal of Inorganic and Nuclear Chemistry, 1976. **38**(5): p. 957-960.

70. Ditroi, F., et al., *Study of activation cross-sections of deuteron induced reactions on rhodium up to 40 MeV.* Nuclear Instruments and Methods in Physics Research Section B: Beam Interactions with Materials and Atoms, 2011. **269**(18): p. 1963-1972.

71. Tárkányi, F., et al., *New cross-sections for production of 103Pd; review of charged particle production routes.* Applied Radiation and Isotopes, 2009. **67**(9): p. 1574-1581.

72. Ohya, T., et al., *A new type of 103Pd/103mRh generator.* Radiochimica Acta, 2025(0).

73. Krol, V., et al., *Cyclotron production of 103Pd using a liquid target.* Nuclear Medicine and Biology, 2023. **118**: p. 108328.

74. Abramov, A., et al., *Isolation of palladium-103 from rhodium targets.* Radiochemistry, 2013. **55**(3): p. 324-327.

75. Xiaoming, W., et al., *Research on Separation, Purification and Quality Control of 103Pd.* Journal of Isotopes, 2023. **36**(6): p. 612-619.

76. Kuznetsova, T., et al., *A Laboratory Setup for Express Electrochemical Dissolution of a Powder Rhodium Target.* Instruments and Experimental Techniques, 2024. **67**(1): p. 153-156.

77. Ohya, T., et al., *Separation of 103Pd from a Rh target using an alloying pretreatment with bismuth.* Radiochimica Acta, 2022. **110**(4): p. 251-258.

78. Afarideh, H., K. Ardaneh, and M. Sadeghi, *Production of Pd 103 seed from Rh targets for brachytherapy.* 2000.

79. Szucs, Z., J. van Rooyen, and J.R. Zeevaart, *Recoil effect on β-decaying in vivo generators, interpreted for 103Pd/103mRh.* Applied Radiation and Isotopes, 2009. **67**(7-8): p. 1401-1404.

80. Zeevaart, J., et al., *Recoil and conversion electron considerations of the 166Dy/166Ho in vivo generator.* 2012.

81. Pineau, J., et al., *Relevance of palladium to radiopharmaceutical development considering enhanced coordination properties of TE1PA.* Chemistry–A European Journal, 2022. **28**(41): p. e202200942.

82. Hojorat, M., et al., *Relevance of Oxocyclam from Palladium (II) Coordination to Radio-pharmaceutical Development pharmaceutical Development.* 2024.

83. Annamalaisamy, G.P., M. Lyczko, and A. Bilewicz, *The radioactive 103 Pd and 109 Pd palladium bipyridyl–bisphosphonate complexes for radionuclide therapy of bone metastatic tumor cells.* RSC advances, 2025. **15**(23): p. 18501-18511.

84. Sporer, E., et al., *Optimized chelator and nanoparticle strategies for high-activity 103Pd-loaded biodegradable brachytherapy seeds.* EJNMMI Radiopharmacy and Chemistry, 2024. **9**(1): p. 92.

85. Fathy, A.A., et al., *Anticancer evaluation and drug delivery of new palladium (II) complexes based on the chelate of alendronate onto hydroxyapatite nanoparticles.* Inorganica Chimica Acta, 2018. **473**: p. 44-50.

86. Cornelissen, B. and K. A Vallis, *Targeting the nucleus: an overview of Auger-electron radionuclide therapy.* Current drug discovery technologies, 2010. **7**(4): p. 263-279.

87. Shen, C.J., et al., *Auger radiopharmaceutical therapy targeting prostate-specific membrane antigen in a micrometastatic model of prostate cancer.* Theranostics, 2020. **10**(7): p. 2888.

88. Sreekumar, S., et al., *Preclinical efficacy of a PARP-1 targeted Auger-emitting radionuclide in prostate cancer.* International journal of molecular sciences, 2023. **24**(4): p. 3083.

89. Filippi, L., L. Urso, and L. Evangelista, *PARP-Targeted radiotheranostics with Auger electrons: an updated overview.* Current Issues in Molecular Biology, 2024. **46**(4): p. 3039-3049.

90. Howell, R.W., *Advancements in the use of Auger electrons in science and medicine during the period 2015–2019.* International journal of radiation biology, 2023. **99**(1): p. 2-27.

91. Wulfmeier, K.M., et al., *Auger Electron-Emitting Radionuclides in Radiopharmaceutical Therapy*, in *Radiopharmaceutical Therapy*. 2023, Springer. p. 409-434.

92. Johnson, R.W., A. Hultqvist, and S.F. Bent, *A brief review of atomic layer deposition: from fundamentals to applications.* Materials today, 2014. **17**(5): p. 236-246.

93. Biri, S., et al., *The atomki accelerator centre.* The European Physical Journal Plus, 2021. **136**(2): p. 247.

94. Kormany, Z. and L. Csedreki, *Verification of the accuracy of a compact beam energy monitor.* Nuclear Instruments and Methods in Physics Research Section A: Accelerators, Spectrometers, Detectors and Associated Equipment, 2025. **1076**: p. 170483.

95. Saidi, P., et al., *Investigation of palladium-103 production and IR07-103Pd brachytherapy seed preparation.* Annals of Nuclear Energy, 2011. **38**(10): p. 2168-2173.

96. Tárkányi, F., et al., *Upgrade of recommended nuclear cross section data base for production of therapeutic radionuclides.* Journal of Radioanalytical and Nuclear Chemistry, 2022. **331**(3): p. 1163-1206.

97. Csik, A., et al., *Analysis of Co/Cu multilayers by SNMS reverse depth profiling.* Vacuum, 2009. **84**(1): p. 141-143.

98. Hampson, R. and R. Walker, *The vapor pressure of palladium.* Journal of Research of the National Bureau of Standards. Section A, Physics and Chemistry, 1962. **66**(2): p. 177.

99. Mendelsohn, J. and J. Baselga, *Status of epidermal growth factor receptor antagonists in the biology and treatment of cancer.* Journal of clinical oncology, 2003. **21**(14): p. 2787-2799.

100. Breeman, W.A., et al., *Radiolabelling DOTA-peptides with 68Ga.* European journal of nuclear medicine and molecular imaging, 2005. **32**(4): p. 478-485.

101. Mehrer, H., *Diffusion in solids: fundamentals, methods, materials, diffusion-controlled processes*. 2007: Springer.

102. Gupta, D., *Diffusion processes in advanced technological materials*. 2010: Springer Science & Business Media.

103. Erdélyi, Z. and D.L. Beke, *Nanoscale volume diffusion: Diffusion in thin films, multilayers and nanoobjects (hollow nanoparticles).* Journal of materials science, 2011. **46**(20): p. 6465-6483.

104. Frenne, D., *Nuclear data sheets for A ¼1 03.* Nucl. Data Sheets, 2009. **110**: p. 2081-2256.

105. RADIOISOTOPES, I. and R. Series, *Guidance for preclinical studies with radiopharmaceuticals.* International Atomic Energy Agency: Vienna, Austria, 2021.

106. de Jong, M., et al., *Tumour uptake of the radiolabelled somatostatin analogue [DOTA0, TYR3] octreotide is dependent on the peptide amount.* European journal of nuclear medicine, 1999. **26**(7): p. 693-698.

107. Connor, N., *What is Radioactive Equilibrium – Definition.* Radiation Dosimetry, 2019.

108. Data, E.N.R., *National Nuclear Data Center.* Brookhaven National Laboratory (http://www. nndc. bnl. gov/exfor/exfor00. htm) and International Atomic Energy Agency, Nuclear Data Services (http://www-nds. iaea. org/exfor/exfor. htm), 2000.

109. Yakushev, E., et al., *An experimental comparison of the K-and L-Auger electron spectra generated in the decays of 140Nd and 111In.* Applied Radiation and Isotopes, 2005. **62**(3): p. 451-456.

110. Zhernosekov, K., et al., *A 140Nd/140Pr radionuclide generator based on physico-chemical transitions in 140Pr complexes after electron capture decay of 140Nd-DOTA.* Radiochimica Acta, 2007. **95**(6): p. 319-327.

111. Roscher, M., G.b. Bakos, and M. Benešová, *Atomic nanogenerators in targeted alpha therapies: Curie's legacy in modern cancer management.* Pharmaceuticals, 2020. **13**(4): p. 76.

112. Mirzadeh, S., K. Kumar, and O.A. Gansow, *The chemical fate of 212Bi-DOTA formed by β-decay of 212Pb (DOTA) 2.* Radiochimica Acta, 1993. **60**(1): p. 1-10.

113. Szilard, L. and T. Chalmers, *Chemical separation of the radioactive element from its bombarded isotope in the Fermi effect.* Nature, 1934. **134**(3386): p. 462-462.

114. Kibèdi, T., et al., *Data needs for Auger electron cascade simulations.* 2013.

115. Kao, H.P., J.R. Abney, and A. Verkman, *Determinants of the translational mobility of a small solute in cell cytoplasm.* The Journal of cell biology, 1993. **120**(1): p. 175-184.

116. Verkman, A.S., *Solute and macromolecule diffusion in cellular aqueous compartments.* Trends in biochemical sciences, 2002. **27**(1): p. 27-33.

117. Alberts, B., *Molecular biology of the cell 4th edition.* (No Title), 2002.

118. Zheng, Y., et al., *Essential role of the voltage-dependent anion channel (VDAC) in mitochondrial permeability transition pore opening and cytochrome c release induced by arsenic trioxide.* Oncogene, 2004. **23**(6): p. 1239-1247.

119. HyperPhysics, *Radioactive Half-Lives and Biological Effects.* n.d.

120. Kim, H.-C. and G.M. Kim, *Radiation pneumonitis following Yttrium-90 radioembolization: A Korean multicenter study.* Frontiers in Oncology, 2023. **13**: p. 977160.

121. Hindié, E., et al., *Palladium-103 (103Pd/103mRh), a promising Auger-electron emitter for targeted radionuclide therapy of disseminated tumor cells-absorbed doses in single cells and clusters,*

with comparison to 177Lu and 161Tb. Theranostics, 2024. **14**(11): p. 4318.

122. Dynkevich, Y., et al., *Tumors, IGF-2, and hypoglycemia: insights from the clinic, the laboratory, and the historical archive.* Endocrine Reviews, 2013. **34**(6): p. 798-826.

123. De Groot, J.W.B., et al., *Non-islet cell tumour-induced hypoglycaemia: a review of the literature including two new cases.* Endocrine-related cancer, 2007. **14**(4): p. 979-993.

IX. Appendix

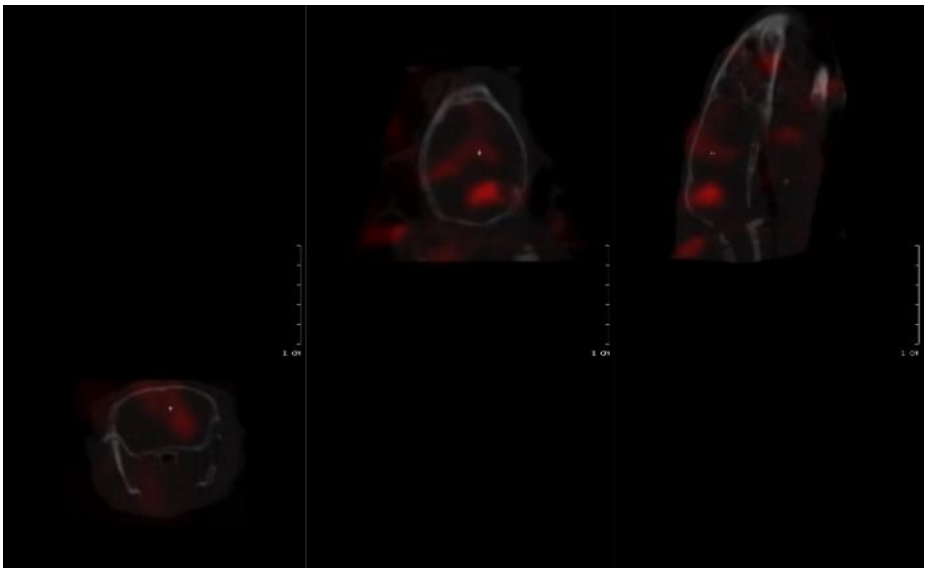

Figure A1. Maximum intensity projection (MIP) SPECT/CT image illustrating cerebral uptake of [^{103}Pd]Pd–PSMA, highlighting involvement of brain folate transport pathways.

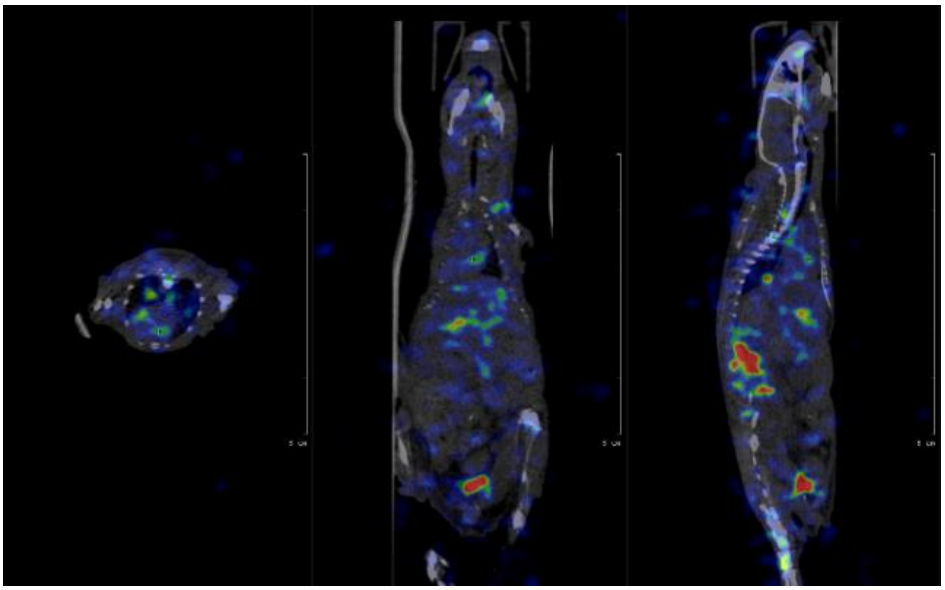

Figure A2. Whole-body MIP SPECT/CT image acquired 10 min post-injection (p.i.) of [^{103}Pd]Pd–cetuximab–NOTA, demonstrating early biodistribution.

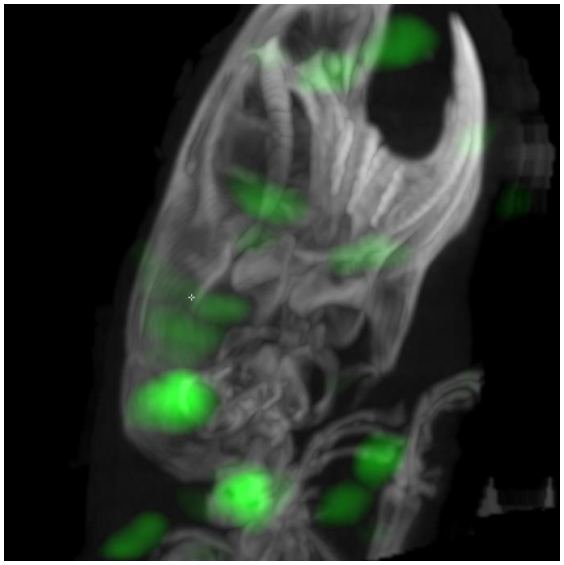

Figure A3. Brain-focused MIP SPECT/CT image of [^{103}Pd]Pd–PSMA, emphasizing uptake patterns associated with folate transporter expression.

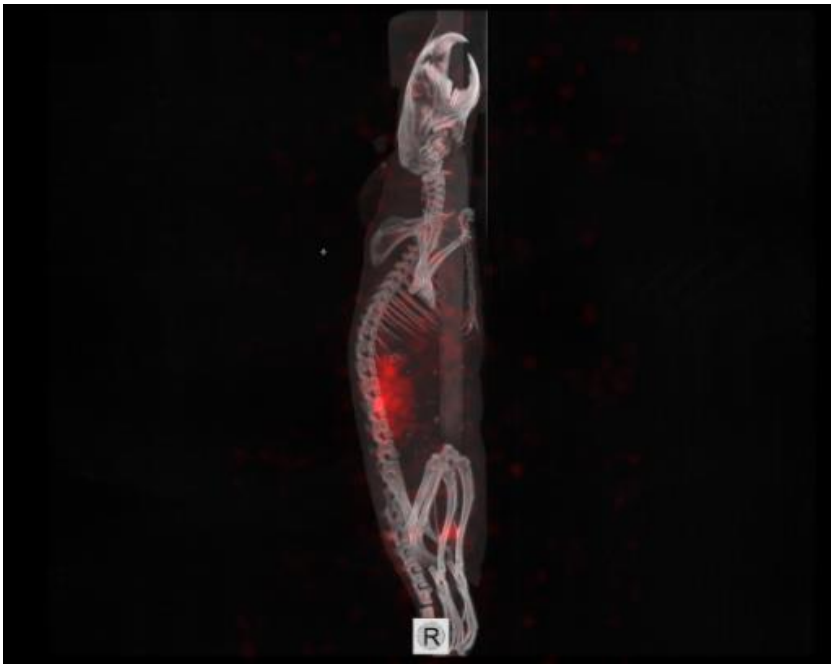

Figure A4. Regional MIP SPECT/CT image (kidney and heart) acquired 10 min p.i. following administration of [^{103}Pd]Pd–cetuximab–NOTA, illustrating early renal clearance and cardiac distribution.

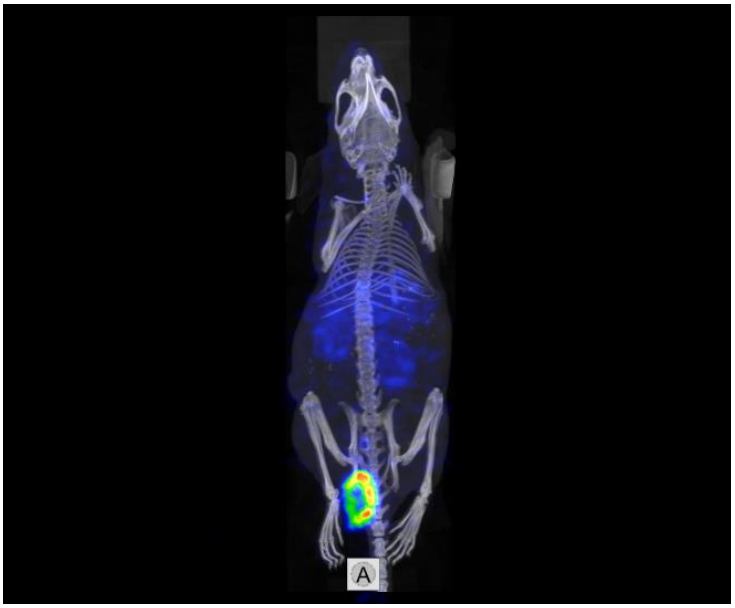

Figure A5. SPECT/CT image acquired 2 h p.i. following administration of [^{103}Pd]Pd–NODAGA–AMBA, demonstrating in vivo biodistribution of the GRPR-targeting radioconjugate.

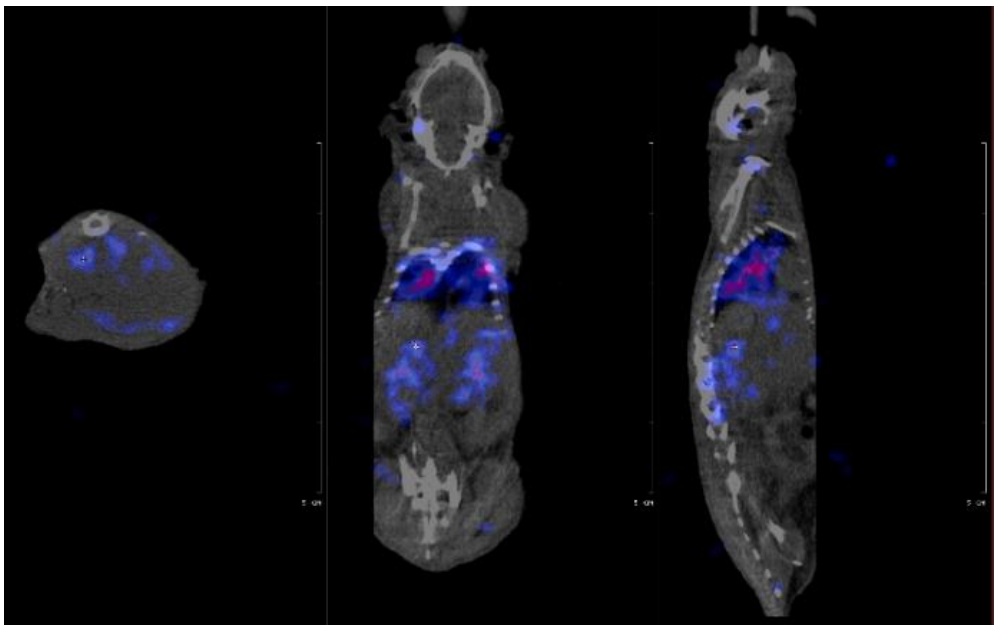

Figure A6. SPECT/CT image acquired 3 days p.i. following administration of [^{103}Pd]Pd–A20–NOTA, highlighting adrenal gland uptake.

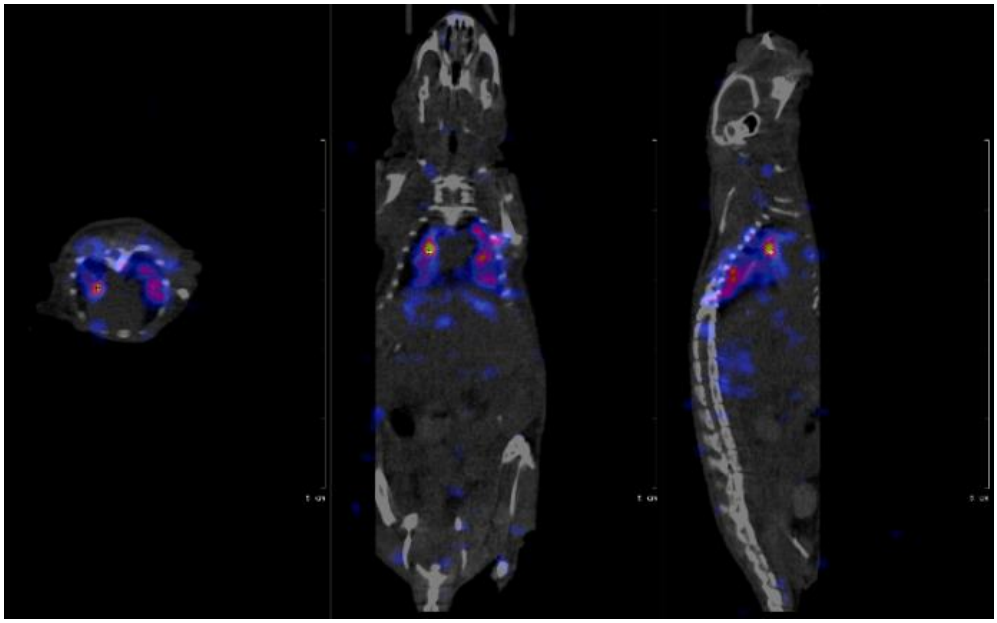

Figure A7. Whole-body SPECT/CT image acquired 3 days p.i. following administration of [^{103}Pd]Pd–A20–NOTA, demonstrating late-phase biodistribution and tracer retention.